SANDIA REPORT

SAND2016-0372
Unlimited Release
Printed January 2016

Quantum Graph Analysis

Peter Maunz, Jonathan D. Sterk, Daniel Lobser, Ojas Parekh, and Ciarán Ryan-Anderson

Prepared by
Sandia National Laboratories
Albuquerque, New Mexico 87185 and Livermore, California 94550

Sandia National Laboratories is a multi-program laboratory managed and operated by Sandia Corporation,
a wholly owned subsidiary of Lockheed Martin Corporation, for the U.S. Department of Energy's
National Nuclear Security Administration under contract DE-AC04-94AL85000.

Approved for public release; further dissemination unlimited.

Sandia National Laboratories

Issued by Sandia National Laboratories, operated for the United States Department of Energy by Sandia Corporation.

NOTICE: This report was prepared as an account of work sponsored by an agency of the United States Government. Neither the United States Government, nor any agency thereof, nor any of their employees, nor any of their contractors, subcontractors, or their employees, make any warranty, express or implied, or assume any legal liability or responsibility for the accuracy, completeness, or usefulness of any information, apparatus, product, or process disclosed, or represent that its use would not infringe privately owned rights. Reference herein to any specific commercial product, process, or service by trade name, trademark, manufacturer, or otherwise, does not necessarily constitute or imply its endorsement, recommendation, or favoring by the United States Government, any agency thereof, or any of their contractors or subcontractors. The views and opinions expressed herein do not necessarily state or reflect those of the United States Government, any agency thereof, or any of their contractors.

Printed in the United States of America. This report has been reproduced directly from the best available copy.

Available to DOE and DOE contractors from
U.S. Department of Energy
Office of Scientific and Technical Information
P.O. Box 62
Oak Ridge, TN 37831

Telephone: (865) 576-8401
Facsimile: (865) 576-5728
E-Mail: reports@adonis.osti.gov
Online ordering: http://www.osti.gov/bridge

Available to the public from
U.S. Department of Commerce
National Technical Information Service
5285 Port Royal Rd
Springfield, VA 22161

Telephone: (800) 553-6847
Facsimile: (703) 605-6900
E-Mail: orders@ntis.fedworld.gov
Online ordering: http://www.ntis.gov/help/ordermethods.asp?loc=7-4-0#online

SAND2016-0372
Unlimited Release
Printed January 2016

Quantum Graph Analysis

Peter Maunz, Jonathan D. Sterk, and Daniel Lobser,
Photonic Microsystem Technologies Department

Ojas Parekh,
Discrete Math and Optimization Department

Ciarán Ryan-Anderson
Non-conventional Computing Technologies Department

Sandia National Laboratories
P.O. Box 5800
Albuquerque, NM 87185-1082
plmaunz@sandia.gov

Abstract

In recent years, advanced network analytics have become increasingly important to national security with applications ranging from cyber security to detection and disruption of terrorist networks. While classical computing solutions have received considerable investment, the development of quantum algorithms to address problems, such as data mining of attributed relational graphs, is a largely unexplored space. Recent theoretical work has shown that quantum algorithms for graph analysis can be more efficient than their classical counterparts.

Here, we have implemented a trapped-ion-based two-qubit quantum information processor to address these goals. Building on Sandia's microfabricated silicon surface ion traps, we have designed, realized and characterized a quantum information processor using the hyperfine qubits encoded in two $^{171}\mathrm{Yb}^{+}$ ions. We have implemented single qubit gates using resonant microwave radiation and have employed Gate set tomography (GST) to characterize the quantum process. For the first time, we were able to prove that the quantum process surpasses the fault tolerance thresholds of some quantum codes by demonstrating a diamond norm distance of less than 1.9×10^{-4}.

We used Raman transitions in order to manipulate the trapped ions' motion and realize two-qubit gates. We characterized the implemented motion sensitive and insensitive single qubit processes and achieved a maximal process infidelity of 6.5×10^{-5}. We implemented the two-qubit gate proposed by Mølmer and Sørensen and achieved a fidelity of more than 97.7%.

Contents

Summary 7
1 Introduction 9
2 Realization and characterization of a two-qubit quantum information processor 11
  2.1 The trapped ion system 11
  2.2 Quantum state preparation and detection 21
  2.3 Single qubit microwave gates 23
  2.4 Single qubit laser gates 31
  2.5 Manipulation of the motional state of a trapped ion 34
  2.6 Two-qubit gate realization 39
  2.7 Two-qubit gate characterization 42
3 Quantum algorithms for our quantum information processor 45
  3.1 Gate model 45
  3.2 A discrete quantum walk on two qubits 48
  3.3 The Quantum Approximate Optimization Algorithm 50
4 Conclusion 57
References 59

Appendix

A GST data of the microwave single qubit gates 65
  A.1 GST results for the “wait” experiment 65
  A.2 GST results for the “BB1 wait” experiment 68
  A.3 GST results for the “BB1 XX” experiment 71
  A.4 GST results for the “BB1 XYXY” experiment 74

Figures

1 Level scheme of $^{171}\mathrm{Yb}^{+}$ 12
2 Sandia Thunderbird trap 13
3 Sandia High-optical-access trap 14
4 Microwave coherence time 17
5 Beatnote lock on fundamental of pulsed laser 19
6 Beatnote lock on 32nd harmonic 19
7 Raman coherence time 20
8 Micromotion characterization using Raman trasitions 22
9 State detection using hsitogram approximation 24
10 Microwave Rabi flopping 25
11 Timescan of BB1 compensated pulse sequence 25
12 Timescan of BB1 compensated multi gate sequence 26
13 Calibration of BB1 pulse offset time 27
14 Markovianity violation as a function of sequence length 29

15 Markovianity violation as a function of sequence length (detail) 30
16 Copropagating Raman Rabi flopping 31
17 Raman sideband cooling 35
18 Sideband cooling 36
19 Motion sensitive Raman Rabi flopping 37
20 Normal modes in a two-ion chain 38
21 Heating rates for the Thunderbird center of mass modes 38
22 Heating rates for the Thunderbird tilt modes 39
23 Heating rates for the HOA-2 trap 40
24 Heating rates as function of principal axes rotiation fro HOA-2 trap 41
25 Mølmer Sørensen Gate, Gate detuning scan 42
26 Mølmer Sørensen Gate, Phase scan 43
27 The Mølmer-Sørensen gate $e^{-i\pi/4\, X\otimes X}$ 46
28 The controlled-Z gate. 47
29 The CNOT gate. 47
30 The gate U'' where the top line represent the clock qubit and the bottom line represents the pointer qubit. 50
31 An example of a *triangle* in a hypergraph, where maximal lines represent hyperedges. The triangle is defined by the three hyperedges, $\{x,y,u\}$, $\{x,z,v\}$, and $\{y,z,w\}$. The dashed hyperedge, $\{u,v,w\}$, is the *foundation* of the triangle. 55
A.1 Markovianity violation 66
A.2 Markovianity violation 69
A.3 Markovianity violation 72
A.4 Markovianity violation 75

Tables

1 Summary of the results from the microwave single qubit GST experiments. 28
2 Summary of GST results for laser-based gates 32
A.1 Comparison of GST estimated gates to target gates 65
A.2 Eigen-decomposition of estimated gates 67
A.3 Comparison of GST estimated gates to target gates 68
A.4 Eigen-decomposition of estimated gates 70
A.5 Comparison of GST estimated gates to target gates 71
A.6 Eigen-decomposition of estimated gates 73
A.7 Comparison of GST estimated gates to target gates 74
A.8 Eigen-decomposition of estimated gates 76

Summary

Within the scope of the Quantum graph analysis (QGA) LDRD, we have investigated quantum graph analysis and have implemented a trapped-ion-based two-qubit quantum information processor for the implementation of quantum graph algorithms. Building on Sandia's microfabricated silicon surface ion traps, we have designed, realized and characterized a quantum information processor using the hyperfine qubits encoded in $^{171}\mathrm{Yb}^{+}$ ions. We have implemented single qubit gates using resonant microwave radiation and have employed Gate set tomography (GST) to characterize the quantum process. For this first time, we were able to prove that the quantum process is above the fault tolerance thresholds of some quantum codes by demonstrating a diamond norm distance of less than 1.9×10^{-4}.

We used Raman transitions in order to manipulate the trapped ions' motion and realize two-qubit gates. We characterized the implemented motion sensitive and insensitive single qubit processes and achieved a maximal process infidelity of 6.5×10^{-5}. We implemented the two-qubit gate proposed by Mølmer and Sørensen and achieved a fidelity of more than 97.7%.

These results demonstrate that Sandia's scalable microfabricated surface ion traps can be used for cutting edge quantum information processing demonstrations.

1 Introduction

In recent years, advanced network analytics have become increasingly important to national security with applications ranging from cyber security to detection and disruption of terrorist networks. While classical computing solutions have received considerable investment, the development of quantum algorithms to address problems, such as data mining of attributed relational graphs, is a largely unexplored space. Recent theoretical work has shown that quantum algorithms for graph analysis can be more efficient than their best known classical counterparts [13, 18, 28].

Outperforming a classical algorithm using a quantum algorithms is a very challenging task and requires the development of a large scalable quantum information processor. Several physical systems, like superconductors [12], silicon quantum dots [3], neutral atoms and trapped ions [33] can be used to encode quantum bits. However to realize a large fault tolerant quantum information processor a system that can implement very high fidelity operations in a way that can be scaled to large numbers of qubits is needed.

The trapped ion system is a promising technology to realize these goals. Quantum information processing in trapped ion systems was developed after Cirac and Zoller proposed the first method to implement a two-qubit gate in the trapped ion system [11]. The proposed two qubit gate was realized soon thereafter [51]. These early results were followed by the realization of many quantum computation primitives like the realization of quantum gates [29, 34, 41], quantum teleportation [6, 42, 39], quantum error correction [43] and small quantum algorithms [9, 35]. More recently the fidelity of two qubit gates has been improved to be close to the threshold for some quantum error correcting codes [4]. Scaling trapped ion quantum information processing by employing sophisticated segmented ion traps was proposed by Kielpinsky et al. [26] in 2002 and the first demonstration of a surface electrode ion trap was achieved in 2006 [45]. Conventional macroscopic ion traps cannot be used to realize complex trapping structures and thus microfabrication of ion traps is essential to reach scalability. While microfabricated traps have been demonstrated and characterized [38, 36, 37, 22], they are still not routinely used for state of the art quantum information processing experiments and there seems to be a hesitation in the community to fully commit to scalable traps.

In this LDRD we have implemented quantum information processes using one and two qubits. We have achieved single qubit operations above some fault-tolerance thresholds and thus have realized the first certifiably fault tolerant single qubit operations. Furthermore, we have implemented a two-qubit quantum gate with a state fidelity of 97.7%. With these results, we have established scalable microfabricated ion traps as a very promising technology to implement a large quantum information processor.

2 Realization and characterization of a two-qubit quantum information processor

2.1 The trapped ion system

In trapped ions qubits can be encoded in two hyperfine states (hyperfine qubit) or a ground state and a meta-stable state (optical qubit). In optical qubits, the two qubit levels are separated by an energy equivalent to an optical photon. In this case the higher energy state is usually a metastable state and its lifetime imposes an absolute limit on the coherence time of the qubit. In contrast, hyperfine states have a virtually infinite lifetime. Furthermore, hyperfine clock states yield qubits with coherence times on the order of several seconds without the need to precisely control the magnetic field fluctuations.

In this work, we have chosen to employ the hyperfine clock state qubit encoded in the $^{171}\mathrm{Yb}^+$ ion. Ytterbium ions have several advantages over other ions species: The hyperfine splitting is large enough to easily implement state selective fluorescence, the Doppler cooling transition at 370 nm is in the near ultra-violet and laser sources are readily available, Raman transitions can be implemented using a laser at 355 nm, a wavelength where ample light is available from tripled YAG lasers. Within the scope of this LDRD we have established quantum information processing at Sandia. We have implemented, characterized and improved the fidelity of single qubit gates using microwave fields as well as motionally insensitive and motionally sensitive laser-based Raman gates. In each case the achieved process fidelities are on par with the best published results for the trapped ion system.

The ytterbium-171 qubit

The $^{171}\mathrm{Yb}^+$ ion features a hyperfine clock state qubit with very low sensitivity to magnetic field fluctuations. The qubit can be easily prepared and detected with high fidelity [40, 38]. The qubit is encoded in the $|0\rangle = |F=0, m_F=0\rangle$ and $|1\rangle = |F=1, m_F=0\rangle$ ground states of the $^2\mathrm{S}_{1/2}$ ground state of the $^{171}\mathrm{Yb}^+$ ion (Figure 1). The qubit transition is only sensitive to the magnetic field to second order $\delta\nu = (310.8)B^2\,\mathrm{Hz}$ where B is given in Gauss.

Doppler cooling, state preparation and state detection are realized using the $^2\mathrm{S}_{1/2}$ to $^2\mathrm{P}_{1/2}$ transition near 811 THz (369.5 nm) as described in detail in [40]. To repump population in one of the $^2\mathrm{D}_{3/2}$, $F=1$ and $F=2$ states a repumper near 320 THz is used. Transitions from the levels populated during all operations into the $^2\mathrm{F}_{7/2}$ are excluded by selection rules. However, the ion can transition into the $^2\mathrm{F}_{7/2}$ state from the $^2\mathrm{D}_{3/2}$ or $^2\mathrm{P}_{1/2}$ when assisted by a collision with another atom or molecule. If the ion reaches the $^2\mathrm{F}_{7/2}$ state, which has a lifetime of 5.4 years, it can be recycled using light at 469 THz (632 nm). In our experiments this happened seldom and we resorted to reloading another ion instead of using the repumping laser. (The longest lifetimes of an ion in the trap of more than 100 h were obtained without this repumping light).

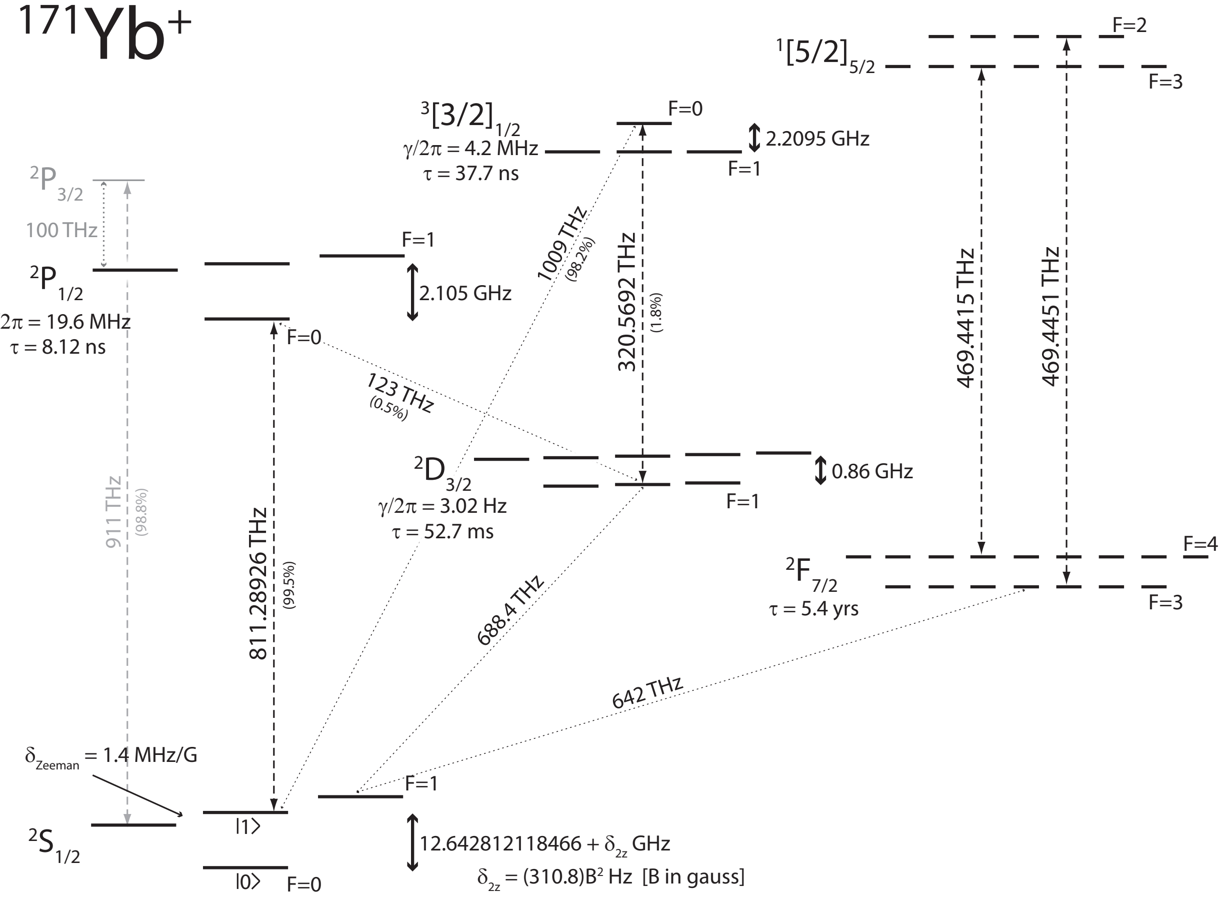

^{171}Yb$^+$
$^1[5/2]_{5/2}$
F=2
F=3
$^3[3/2]_{1/2}$
γ/2π = 4.2 MHz
τ = 37.7 ns
F=0
F=1
2.2095 GHz
^{2}P$_{3/2}$
100 THz
^{2}P$_{1/2}$
γ/2π = 19.6 MHz
τ = 8.12 ns
F=1
2.105 GHz
F=0
1009 THz
(98.2%)
320.5692 THz
(1.8%)
469.4415 THz
469.4451 THz
123 THz
(0.5%)
^{2}D$_{3/2}$
γ/2π = 3.02 Hz
τ = 52.7 ms
0.86 GHz
F=1
911 THz
(98.8%)
811.28926 THz
(99.5%)
688.4 THz
^{2}F$_{7/2}$
τ = 5.4 yrs
F=4
F=3
642 THz
δ$_{Zeeman}$ = 1.4 MHz/G
^{2}S$_{1/2}$
|1⟩
F=1
|0⟩
F=0
12.642812118466 + δ$_{2z}$ GHz
δ$_{2z}$ = (310.8)B^2 Hz [B in gauss]

Figure 1. Level scheme of ^{171}Yb$^+$. The qubit is encoded in the $|0\rangle = |F = 0, m_f = 0\rangle$ and $|1\rangle = |F = 1, m_f = 0\rangle$ hyperfine clock states states of the ^{2}S$_{1/2}$ ground state of singly ionized 171-ytterbium atom. Excitation to the ^{2}P$_{1/2}$ excited state using light near 811 THz is used for Doppler cooling, state preparation and state detection. For Doppler cooling the second sideband imprinted by a 7.37 GHz electro-optical modulator recovers population from the $|0\rangle$ dark state. State preparation is done by adding a 2.1 GHz sideband resonant with the ^{2}S$_{1/2}$, $F = 1$ to ^{2}P$_{1/2}$, $F = 1$ transition to the Doppler laser. For state detection no sidebands are applied.

Sandia surface ion traps

Sandia microfabricated ion traps are fabricated on a silicon chip. For best trap performance, gold-coated aluminum electrodes are used and the oxide dielectric separating metal layers is shielded from the ions to prevent charging effects. Two different Sandia microfabricated surface traps have been used for experiments in the scope of the LDRD. For initial experiments, we used the Sandia Thunderbird trap (Figure 2) [50]. This trap uses two metal layers, the routing of all control electrodes is in one of these metal layers which limits the available trap topology and trap geometries. However, most experiments were done in the Sandia High Optical Access trap (HOA-2) (Figure 3). Both traps feature a long linear section with through wafer slot. In addition, the HOA-2 trap has two Y-junctions [32] and transitions between the slotted and above-surface regions.

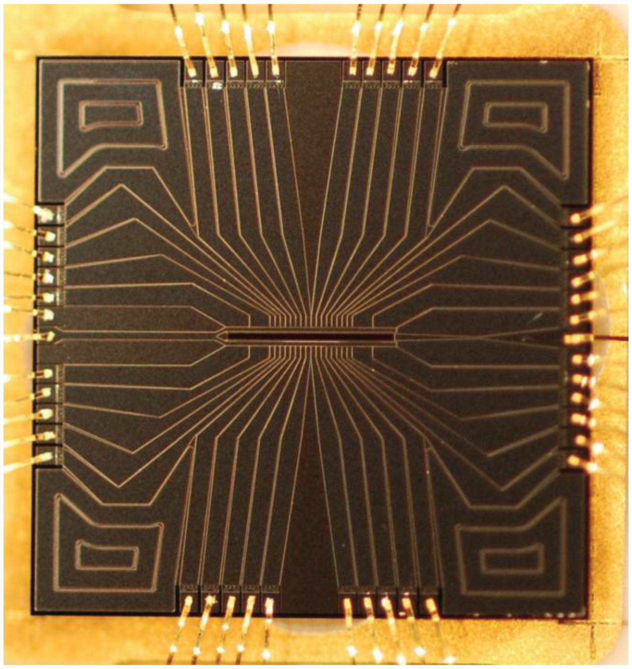

Figure 2. Sandia Thunderbird microfabricated surface ion trap. The Thunderbird is a linear surface trap with through chip slot. The trap is fabricated using two metal layers. Therefore the routing of the electrodes to the bondpads is visible. Furthermore, only simple trap topologies are possible as all electrodes need to be connected to the wirebond pad in the same metal layer.

Advantages of the HOA trap over the Thunderbird trap are:

- increased optical access, a 370 nm beam can be focused to $< 4\,\mu$m skimming the surface and to $< 2\,\mu$m when applied through the slot.

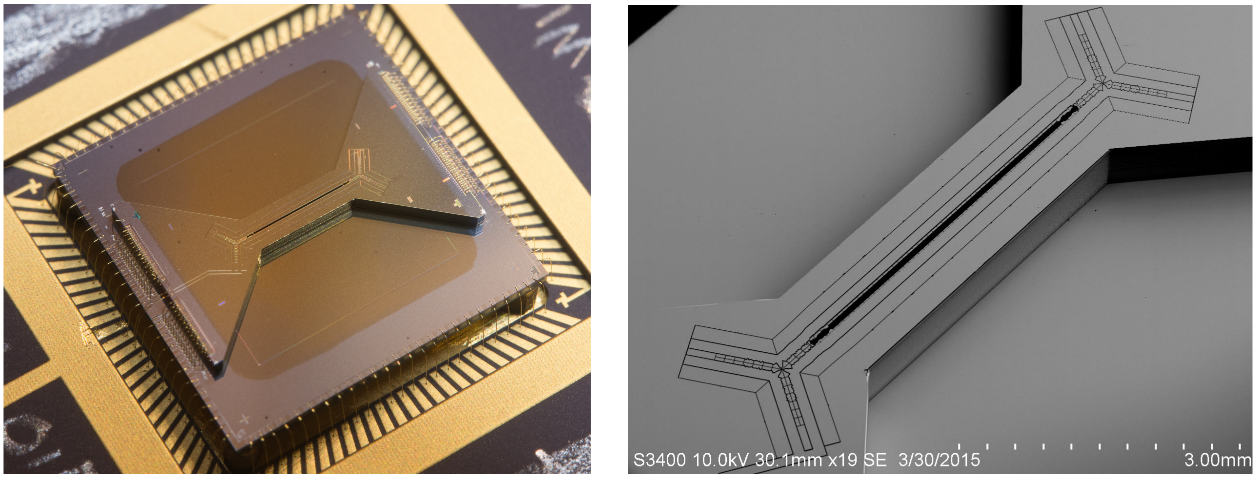

Figure 3. Sandia High-optical-access microfabricated surface ion trap. *left:* Photograph *right:* Scanning electron micrograph. The trap is fabricated using a 4 metal layer process. Where lower metal layers are used for routing. This makes it possible to segment the control electrodes closest to the ions and thus improve control voltage efficiacy. Furthermore, this traps includes transitions between slotted and above-surface regions and two Y-junctions.

- characteristic distance $\approx 140\,\mu\text{m}$. Leading to higher trap frequencies resulting in better ground state cooling and reduced ion heating.
- smaller intrinsic heating rates ($\approx 30\,{}^{\text{quanta}}/_{\text{s}}$ for a radial mode with frequency 3 MHz.)

The Thunderbird and HOA-2 traps use one rf voltage and 42 (94) dc control voltages, respectively. Both traps are mounted on interposer chips. The interposer chips include trench capacitors with a capacitance of 1 nF on all DC control signals. They are used to reduce pick-up of the rf voltage on dc control voltages. In the case of the HOA-2 trap, the interposer also routes the DC control signals from the ends of the bow-tie shaped HOA-2 chip to the full perimeter of the interposer chip, where the bondpads of the package are located. Microfabricated surface traps require careful handling, they may only be handled in a clean environment (ideally a cleanroom) to prevent contamination with particulates which could lead to shorting of electrodes and will impact the heating rates of the trap. The chambers used in these experiments did undergo a rigorous cleaning and were assembled in a cleanroom.

Vacuum system

To trap ions the ion trap has to be located in a vacuum chamber. Because background collisions can lead to ion loss, melting of ion crystals and collision-mediated transitions, it is very important to conduct experiments in ultra-high vacuum ($< 10^{-10}$ mbar). The vacuum chambers used for these experiments use a spherical octagon chamber which enables the placement of imaging optics with a working distance of ≈ 12 mm from a re-entrant viewport. Furthermore, 6 of the 8 ports on the perimeter of the chamber can be used to introduce laser beams. Two ports are used for pumping and a feed-through to introduce the rf voltage needed for trapping. 94 DC control voltages are introduced via a feedthrough at the bottom of the chamber. The chamber is evacuated using turbomolecular pumps. To reduce the vacuum pressure, the chamber undergoes a vacuum bake at 200°C for about 5 days. During operation, the vacuum is maintained by an ion pump and a titanium sublimation pump.

Laser system

To trap and Doppler cool ytterbium ions the following laser frequencies are used:

- 370 nm: Doppler cooling, state preparation, state detection
- 398 nm: Photo-ionization
- 935 nm: Depopulation of the $^2D_{3/2}$ states
- 630 nm: Depopulation of the $^2F_{7/2}$ states. Optional, not used here.

370 nm **Doppler cooling laser.** The 370 nm light used for Doppler cooling, state preparation and state detection is generated by a amplified and frequency doubled diode laser. The laser frequency is locked by sending some of the fundamental light at 740 nm on a transfer cavity. The transfer cavity itself is locked to a rubidium vapor cell stabilized 780 nm laser. At the output of the 370 nm laser, the light first passes through an acoustooptic modulator (AOM) and a single mode fiber. Then the light is split in three separate beams for Doppler cooling, state preparation and state detection. The Doppler cooling light passes through a resonant 7.37 GHz electrooptical modulator (EOM). The second sideband of this EOM at 14.7 GHz is used to de-populate the $|0\rangle$ state during cooling. The cooling light passes through an AOM before being coupled into a single mode fiber for delivery to the trap. Fiber paddles are used to adjust the polarization of the light for maximal fluorescence. The light for state preparation passes through a 2.1 GHz EOM and a AOM before being combined with the cooling light with orthogonal polarization. The light for state detection only passes through an AOM and is then coupled into a dedicated optical fiber for delivery to the trap. Here again fiber paddles are used to adjust the polarization.

Separating the beams for cooling, state preparation and state detection was necessary because the EOMs did distort the beam when being switched. Thus the EOMs are driven continuously while the AOMs are used for switching the light. Without the AOM at the laser output and the extra mode cleaning by the first fiber, the extinction achieved using the AOMs was not sufficient and limited the coherence time to $T_1 = 300$ ms (Figure 4). After adding the additional AOM and fiber the T_1 time does not limit the coherence time any more and a coherence time of $T_2^* = 3$ s was measured.

398 nm **Photo-ionization laser.** For photo-ionization a 398 nm direct diode laser is used. The laser is locked to a wavemeter (resolution 10 MHz).

935 nm **Repumper.** For de-population of the $^2\mathrm{D}_{3/2}$states a direct diode laser is used. The laser is locked to a wavemeter and passes through a fiber EOM to imprint sidebands at 3.06 GHz. The sideband is necessary to de-populate the $^2\mathrm{D}_{3/2}$, $F = 2$ state. This state is populated if after off-resonant excitation to the $^2\mathrm{P}_{1/2}$, $F = 1$ state the ion decays to $^2\mathrm{D}_{3/2}$, $F = 2$ state.

Microwave signal generation

The microwave signal at 12.642 GHz is generated using a disc resonator oscillator (DRO) at 12.6 GHz and single sideband (SSB) modulating the output with the signal from a direct digital synthesizer (DDS) at 42 MHz. The DRO as well as the DDS are locked to a 10 MHz rubidium frequency standard. A high isolation rf switch at the output of the DDS is used to switch the microwave signal. An additional microwave switch at the output of the SSB modulator was first used and later abandoned for its slow (10 μs) ringing when switched which severely impacted the fidelity of the microwave gates. To measure the coherence time of the microwave signal with respect to the qubit transition a Ramsey experiment was used. After Doppler cooling and state preparation, a $\pi/2$ microwave pulse is followed by an adjustable wait time. A second microwave $\pi/2$ pulse with adjustable phase is used before state detection. The contrast of the oscillation obtained as a function of the analysis phase is extracted. The contrast is plotted as a function of the wait time in Figure 4. If the de-coherence is mostly due to de-phasing, it is best described by Gaussian decay [40]. Here, we achieved a coherence time $T_2^* = 3\,\mathrm{s}$.

Raman laser system

Resonant microwave radiation is one way to implement single qubit gates. However, it is hard to confine microwave radiation to a small region in order to address individual ions. Individual addressing can be achieved in frequency space by shifting the resonant frequency of ions. However, the ability to shift the qubit frequency is not commensurable with an intrinsically stable qubit. Raman lasers can be used to address individual ions as well as address the motion of ions and implement two-qubit gates [20, 19]. Microwave gradient fields can also be used to implement two-qubit gates [41] if very strong microwave gradient fields are available.

Raman transitions are two-photon transitions via a virtual state that are resonantly enhanced by using a virtual state close to an exited ion state. The further detuned the virtual state is from the excited state, the lower the excitation probability to the excited state and the lower the decoherence from the resulting spontaneous emission. However, the further detuned the virtual state is from the excited state the more power is necessary. While spontaneous emission is inverse proportional to the square of the detuning, the Raman Rabi frequency scales inverse proportionally with the detuning. Thus, the spontaneous emission per π pulse drops linearly with the detuning. Another

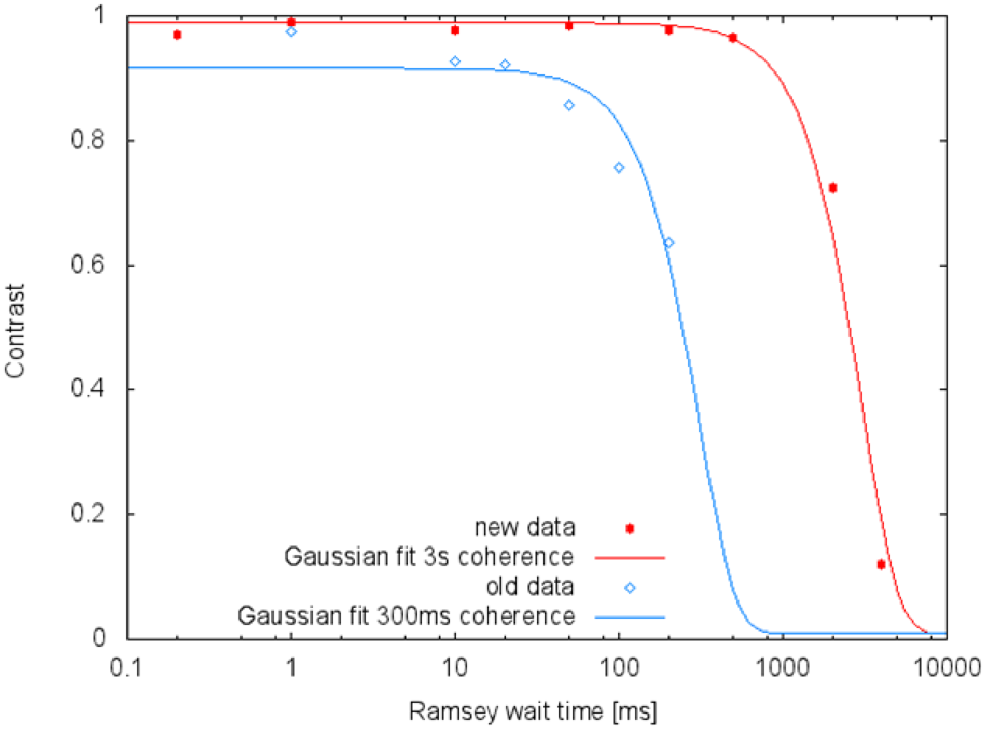

Figure 4. Microwave coherence time. A Ramsey experiment is used to measure the T_2^* coherence time of the qubit. An initial $\pi/2$ preparation pulse is followed by an adjustable wait time and a $\pi/2$ analyzing pulse with adjustable phase. Ideally this results in an oscillation with a contrast of 1. In this graph the contrast of the resulting oscillation is plotted as a function of the wait time on a logarithmic scale. De-phasing, the origin of the reduction of contrast is best described by a Gaussian envelope. A fit to a Gaussian function of the first data resulted in a coherence time of 300 ms after improvements to the experimental setup the coherence time was increased to 3 s, long compared to a typical gate time of 40 μs.

unintended effect of the Raman laser are differential Stark shifts that change the qubit detuning as a function of laser intensity. In ytterbium there the optimal Raman laser wavelength with respect to scattering and Stark shifts is at a wavelength of 355 nm where the detuning from the closest excited state is more than 30 THz [31]. At this wavelength plenty of power is available from industrial 355 nm tripled YAG lasers. (Our laser system produces an average power of 3.7 W, but pulsed 355 nm YAG systems are available with average power of 20 W.)

To drive Raman transitions between the two qubit levels, two phase locked lasers with a frequency difference of 12.642 GHz are necessary. Phase-locking two lasers to a differential linewidth $\ll 1\,\mathrm{Hz}$ is quite challenging and frequency shifting a beam by 12.6 GHz cannot be achieved efficiently. However, lines from the frequency comb generated by a pulsed laser can be used to drive these Raman transitions easily and efficiently. The repetition rate of the laser should lead to a frequency spectrum broader than the 12.6 GHz hyperfine splitting. Here, we are using the frequency comb generated by the pulsed laser. This means we are using many laser pulses. This is also known as the slow regime. In contrast one can use single or few pulses to achieve transitions on picosecond timescales and realize two-qubit gates faster than the trap period [17].

To this end we choose the repetition rate of the pulsed laser to *not be commensurable* with the 12.642 GHz frequency splitting — otherwise we would not be able to control the Raman interaction. We then split the laser beam in two independent beams and shift each with an AOM. Raman Rabi oscillations can be driven if we choose the difference of the two AMO frequencies such that

$$\nu_{\mathrm{qubit}} = n\nu_{\mathrm{rep}} + \Delta\nu_{AOM}. \tag{1}$$

Here ν_{qubit} is the frequency difference of the two hyperfine qubit levels, ν_{rep} is the repetition rate of the laser and $\Delta\nu_{AOM}$ is the frequency difference of the two AOMs. We are using an industrial picosecond pulsed laser which does *not* provide a method to stabilize the repetition rate. However, we do not rely on a stabilized repetition rate, we just need to fulfill equation (1). We can achieve this by dynamically adjusting the frequency difference of the AOMs as

$$\Delta\nu_{AOM} = \nu_{\mathrm{qubit}} - n\nu_{\mathrm{rep}}. \tag{2}$$

We can realize this by measuring the repetition rate ν_{rep} and adjusting one AOM frequency by $n\nu_{\mathrm{rep}}$. We first realized this beatnote lock by measuring the fundamental of the repetition rate as described in Figure 5. We characterized the quality of the lock by measuring the coherence time using a Ramsey experiment. The data are shown in green in Figure 7. Up to $100\,\mu$s delay time we see full Ramsey contrast. Then the contrast drops to $\approx 85\%$ for delay times between 1 ms and 1 s. This is indicative of a frequency that is locked as intended, however the phase excursions while locked are large enough to reduce the Ramsey coherence to 85%. A small phase uncertainty in the measurement of the fundamental repetition rate can cause this as the frequency adjustment has to multiplied by 105 when comb lines 105 lines apart are to be used for the Raman transitions. The lock can be improved by obtaining a steeper error signal by measuring the frequency of harmonics of the repetition rate. The photodiode measuring the repetition rate will have harmonics of the repetition rate up to and beyond the 12.6 GHz hyperfine splitting. As we go to higher and higher harmonics the error signal becomes steeper. However, the signal to noise of the harmonics decreases. Therefore, there is a optimal harmonic for which the harmonic number times the signal

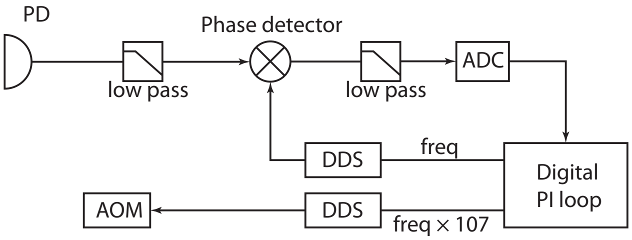
PD
Phase detector
low pass
low pass
ADC
DDS
freq
Digital
PI loop
AOM
DDS
freq × 107

Figure 5. Beatnote lock of the pulsed laser based on measurement of the fundamental of the repetition rate. The instantaneous power of the pulsed laser is measured using a fast photodiode (PD). A low-pass filter suppresses higher harmonics of the repetition rate. This signal is mixed with the sine wave generated by a direct digital synthesizer (DDS). The resulting low frequency signal is digitized using a $1MS$ analog to digital converter (ADC). A digital proportional integral (PI) feedback loop adjusts the DDS frequency to track the repetition rate of the laser. With $\nu_{rep} = \nu_1 + \Delta\nu$. Because the Raman transitions are driven by comb lines in the distance of 107 repetition rates the second DDS is adjusted by $107 \times \Delta\nu$.

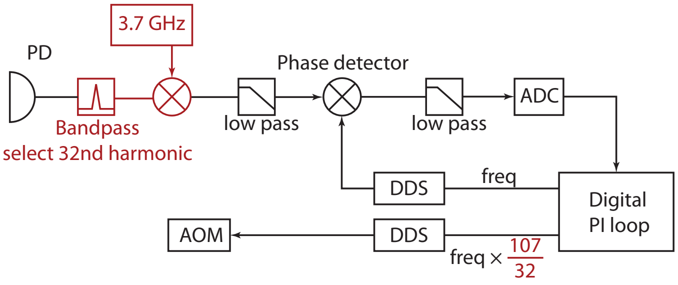
3.7 GHz
PD
Bandpass
select 32nd harmonic
Phase detector
low pass
low pass
ADC
DDS
freq
Digital
PI loop
AOM
DDS
freq × 107/32

Figure 6. Beatnote lock on the 32nd harmonic of the repetition rate. A fast photodiode (PD) measures the instantaneous power of the pulsed laser. A bandpass is used to pass only the 32nd harmonic of the laser repetition rate close to 3.8 GHz. This signal is mixed with a local oscillator near 3.7 GHz. The resulting low frequency signal near 100 MHz then changes with $32\Delta\nu_rep$ and thus amplifies the repetition rate fluctuations. As described in Figure 5, a direct digital synthesizer (DDS) is then used to track this frequency. The second DDS is then adjusted with $\frac{107}{32}\Delta\nu$.

to noise is optimal. For our photodiode and electronics this is approximately at the 32nd harmonic close to 3.7 GHz. The beatnote lock based on this harmonic is described in Figure 6. When employing this locking scheme the coherence time was increased to 1 s (Figure 7). Between these two measurements we changed our master oscillator from a cesium primary frequency standard to a rubidium frequency standard, as a consequence of the reduced stability of our master clock the coherence time was reduced from 3 s to 1 s.

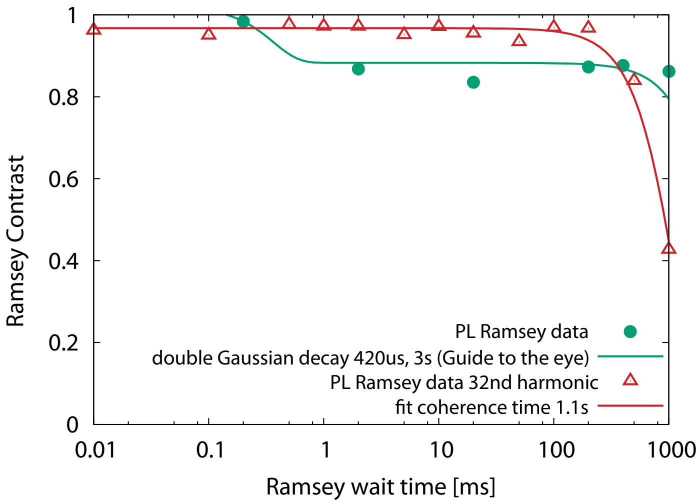

Figure 7. The coherence time of the Raman laser is measured in the same way as the microwave coherence time (see Figure 4). With the pulsed laser beatnote lock implemented on the fundamental of the repetition rate (green data), the Ramsey contrast is close to 1 up to 100 μs but drops to $\approx 85\%$ at 1 ms and remains at $\approx 85\%$ up to wait times beyond 1 s. This behavior is indicative of the beatnote following a microwave reference with more than 1 s coherence time, however, the phase uncertainty of the lock leads to a reduced contrast. The data shown in red is for a beatnote lock using the 32nd harmonic of the repetition rate. Here, the 32 times steeper error signal allows one to tighten the lock and maintaining full contrast out to about 1 s. (The reduction of the coherence time from ≈ 3 s to ≈ 1 s is attributed to the switch to a less precise master clock).

Trap characterization

In a linear rf Paul trap, the ion is trapped in two (lateral) dimensions by a ponderomotive potential. In the third (axial) dimension the trapping potential is provided by electrostatic forces. The motion of the ion in the ponderomotive potential has a component at the trap frequency, but also has “micromotion” at the rf frequency. The micromotion amplitude is approximately

$$a_{\mu mot} \approx qd, \tag{3}$$

where q is the trap stability parameter and d is the distance from the rf node. The stability parameter is approximately $q \approx 2\sqrt{2}\frac{\omega}{\Omega}$. Here ω is the secular frequency of the ion in the trap and Ω is the rf drive frequency. Homogeneous electric fields are used to compensate background fields and move the trapped ion to the rf node. There a several established methods to characterize micromotion:

1. Measuring the lineshape of the Doppler cooling transition. Micromotion will lead to sidebands at the rf drive frequency. As this method relies on the Doppler effect it only is sensitive to micromotion in the direction of the laser beam.

2. Measuring correlations between scattered photons and the rf phase. As method 1. this method only detects micromotion in the direction of the laser beam.

3. Exciting the ion motion by adding a sideband to the rf drive. If the sideband is detuned from the rf drive frequency by the trap frequency, the ion’s motion is driven and can be observed by a change in fluorescence. If the principal axes are *not* perpendicular to the Doppler cooling laser this method is sensitive to micromotion in the direction of both lateral principal axes.

4. Driving motionally sensitive qubit transitions on the micromotion sideband. This method is only sensitive to micromotion along the laser beam. However, it is the only method in which a single scan can be sufficient to determine the field with minimal micromotion. See Figure 8.

2.2 Quantum state preparation and detection

Quantum state preparation is achieved by adding a 2.1 GHz sideband to the Doppler cooling light and driving the transition from $^2\mathrm{S}_{1/2}$, $F = 1$ to $^2\mathrm{P}_{1/2}$, $F = 1$. From $^2\mathrm{P}_{1/2}$ the ion has a 1/3 probability to drop into the $|0\rangle$ state. After it has reached $^2\mathrm{S}_{1/2}$, $F = 0$ it does not scatter light anymore. Because state preparation relies on spectral purity, the $|0\rangle$ state can be easily prepared with high fidelity $> 99.5\%$.

Quantum state detection relies on the scattering of light of the $^2\mathrm{S}_{1/2}$, $F = 1 \leftrightarrow {}^2\mathrm{P}_{1/2}$, $F = 0$ transition. While the repumping from the $^2\mathrm{D}_{3/2}$ state is done in a way that the ion is prevented from dropping into the $|0\rangle$ state by selection rules, off-resonant excitation to the $^2\mathrm{P}_{1/2}$, $F = 1$ state can turn a bright state into the dark state. Thus, only a finite number of photons can be generated for state detection. State detection fidelity can be improved and the necessary detection time can be reduced by increasing the fraction of light collected [38].

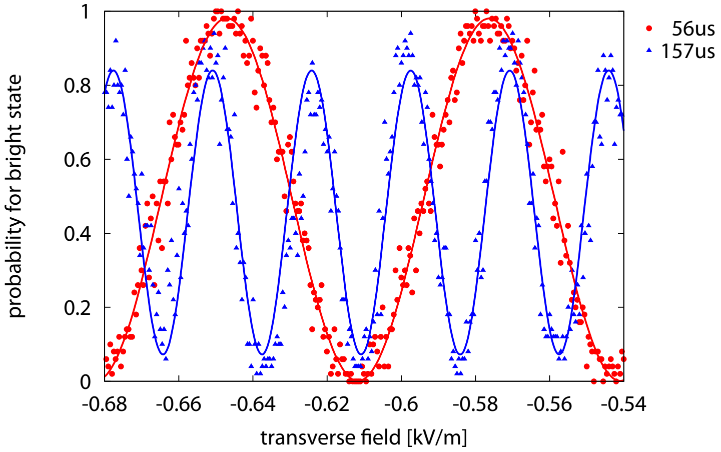

Figure 8. Micromotion characterization using Raman transitions on the micromotion sideband of the transition carrier. If the ion experiences micromotion, it is possible to drive Raman transitions at the frequency $\omega_{\rm carrier} + \omega_{\rm rf}$ where $\omega_{\rm carrier}$ is the frequency of the carrier transition between the qubit states and $\omega_{\rm rf}$ is the rf drive frequency. If the ion is located at the rf node, this transition is suppressed. Here, we plot the probability to find the ion in the $|1\rangle$ state as a function of the lateral electrical field after $56\,\mu$s and $157\,\mu$s for the red and blue data, respectively. For an offset field of $-610\,{\rm V/m}$ transitions are suppressed and the ion is positioned at the rf node.

Threshold detection

For threshold detection the scattered photons of a single detection event are counted. If the number exceeds the threshold, the ion is measured in the bright state $|1\rangle$, otherwise it is detected in the dark state $|0\rangle$. If the ion is in the dark state, only dark- and background counts are registered. In the bright state a Poissonian distribution of the number of detected photons is expected. Off-resonant pumping to the dark state leads to a “bleeding” of this distribution to smaller numbers of detected photons. For an average number of 10 detected photons the overlap between the two distributions can be reduced to less than 1% for our imaging and photo detection system. When considering two ions, the distributions for 1 and 2 bright ions have a considerable overlap which severely limits the fidelity of a single shot detection of the number of bright ions. A better alternative is to image multiple ions on independent detectors and use standard threshold detection on each detector. If that is not possible — in our case the aberrations of the imaging system resulted in prohibitive crosstalk between neighboring ions — then it is still possible to determine the average number of events with 1 or 2 bright ions in an ensemble.

Fitting to measured histograms

To determine the average number of events with 0, 1 or 2 ions bright in an ensemble we use the following procedure. First, we measure histograms of detection events with 0, 1 and 2 bright ions. For this calibration we used at least $10,000$ events per histogram. Then we take a histogram for the experiment to be analyzed and approximate the measured histogram with superpositions of the calibration histograms. While this method does *not* allow one to determine the result of a single experiment it performs well on ensembles. In Figure 9, the result of a 2-ion microwave Rabi flopping is shown. The data can be approximated by theoretical curves using only the π-time as fit parameter.

2.3 Single qubit microwave gates

Resonant microwave radiation can be used to realize single qubit gates.

Implementation of single qubit microwave gates

At the beginning of every experiment, the ion is Doppler cooled for at least $2\,\mathrm{ms}$. The scattered light during Doppler cooling is used to verify that a cold ion is present in the trap. A $5\,\mu\mathrm{s}$ pulse of light resonant with the ${}^2\mathrm{S}_{1/2}$, $F=1 \leftrightarrow {}^2\mathrm{P}_{1/2}$, $F=1$ transition is then used to initialize the ion in the $|0\rangle$ state. After state initialization, square pulses of resonant microwave radiation are applied to realized quantum gates. Finally, the qubit state is measured by applying light resonant with the ${}^2\mathrm{S}_{1/2}$, $F=1 \leftrightarrow {}^2\mathrm{P}_{1/2}$, $F=0$ transition. The ion is projected on either $|0\rangle$ or $|1\rangle$. If it is projected on $|1\rangle$, the incident light is scattered by the ion, if it is projected to $|0\rangle$ no light is scattered. From

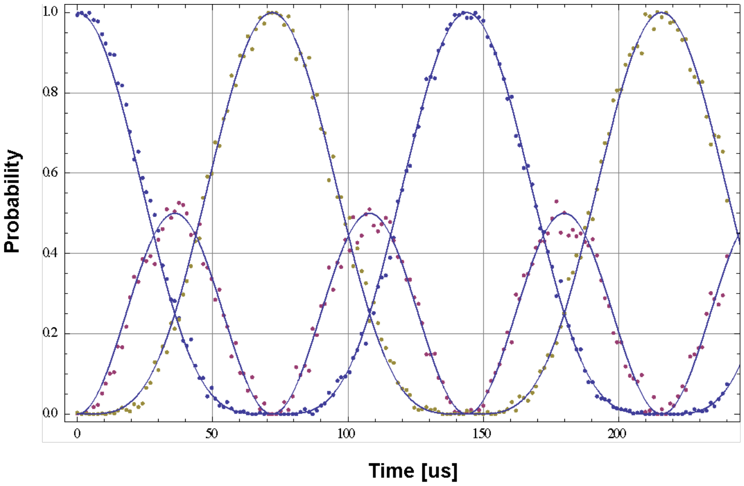

Figure 9. State detection using histogram approximation. Two ions are subject to microwave radiation resonant with the qubit transition. The quantum state of the two qubits is measured using histogram approximation and plotted as a function of the duration of the microwave pulse. Blue: both ions dark, Red: one ion bright, Green: both ions bright. A single parameter, the π-time, is sufficient to describe the measured data.

the number of photons detected within a 1 ms time interval we can determine the quantum state with approximately 98.5% fidelity.

In the simplest case the qubit manipulation pulse is a single square pulse of microwave radiation resonant with the qubit transition. Depending on the length of the pulse, the population oscillates between $|0\rangle$ and $|1\rangle$. These Rabi-oscillations are shown in Figure 10. If the duration of the pulse is chosen to transfer the population from $|0\rangle$ to $|1\rangle$ ($\approx 25\,\mu$s in Figure 10) we call this a π-pulse. A pulse of half the duration, a $\pi/2$-pulse, leaves the qubit in a superposition state $|\psi\rangle = \frac{\sqrt{2}}{2}(|0\rangle + |1\rangle)$.

Because the derivative of the Rabi flopping curve is largest near the superposition state, the fidelity of this operation depends critically on a stable microwave amplitude. To reduce the dependency of the fidelity of the entangled state on intensity fluctuations broadband (BB) pulses have been devised [53, 30] that can reduce the dependency by an arbitrary order. An example of a single BB1 pulse is shown in Figure 11. The BB1 sequence for a $\pi/2$ pulse around σ_x ($R_0(\pi/2)$) is $R_{\arccos(-1/8)}(\pi)R_{3\arccos(-1/8)}(2\pi)R_{\arccos(-1/8)}(\pi)R_0(\pi/2)$ where $R_\phi(\theta)$ is a rotation about the axis with angle ϕ to the σ_x axis with rotation angle θ.

The vanishing derivative close to the entangled state is clearly visible is Figure 11. An example of 5 consecutive BB1 pulse sequences is given in Figure 12. Here again the region with small derivative is seen at the correct $\pi/2$-time of $16\,\mu$s. However, the probability to find the ion in the bright state is only 30% instead of the expected 50%. While the BB1 pulse sequence reduces the dependency on the overall intensity stability of the microwave radiation, the BB1 pulse sequence

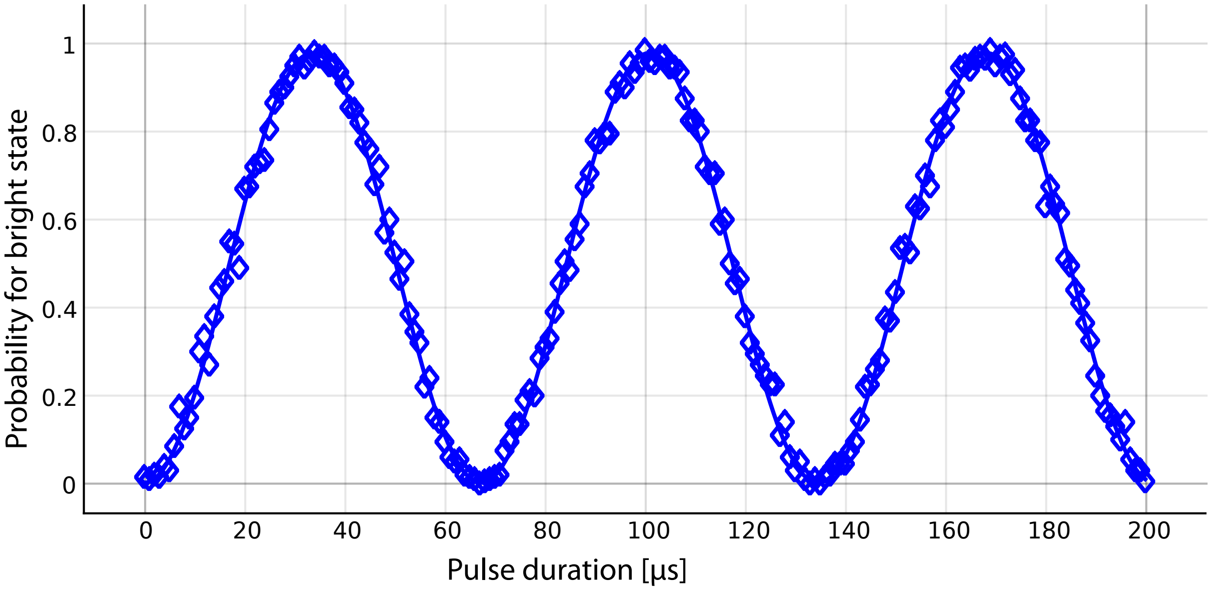

Figure 10. Microwave Rabi flopping.

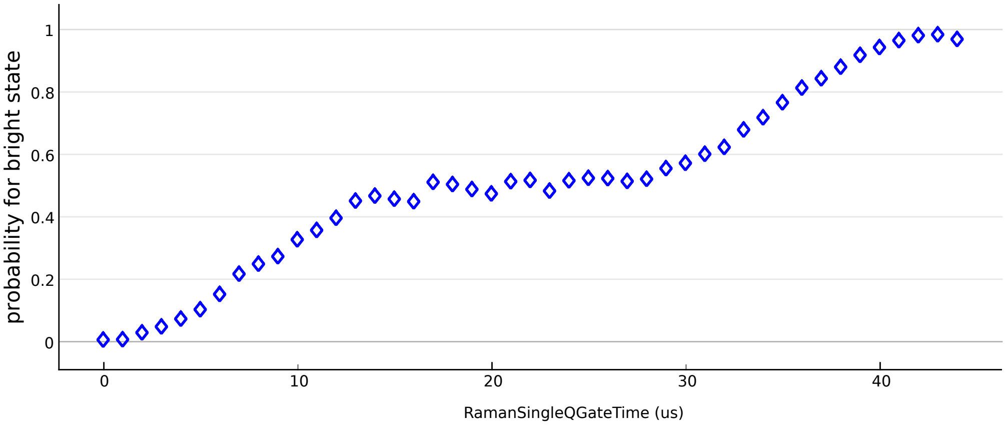

Figure 11. Probability to find the ion in the $|1\rangle$ state as a function of duration of a BB1 compensated broadband pulse. The correct pulse time is approximately $22\,\mu$s. In contrast to simple Rabi flopping where the slope is highest when the ion is in the superposition state $|0\rangle + |1\rangle$, we see a vanishing slope. This demonstrates the ability of the broadband sequence BB1 to compensate for slow fluctuations on a timescale slower than the pulse sequence.

is quite sensitive to the relative duration of the $\pi/2$, π and 2π constituent pulses. To compensate imperfections of the switching characteristics, a constant offset is added phenomenologically to all four constituent pulses. Then 101 (103) BB1 composite gate pulses are applied. As can be seen in Figure 13, the expected probability of 50% is reached at an offset of 85 ns for both, 101 and 103 gate pulses. Therefore, this offset is used for the experiment.

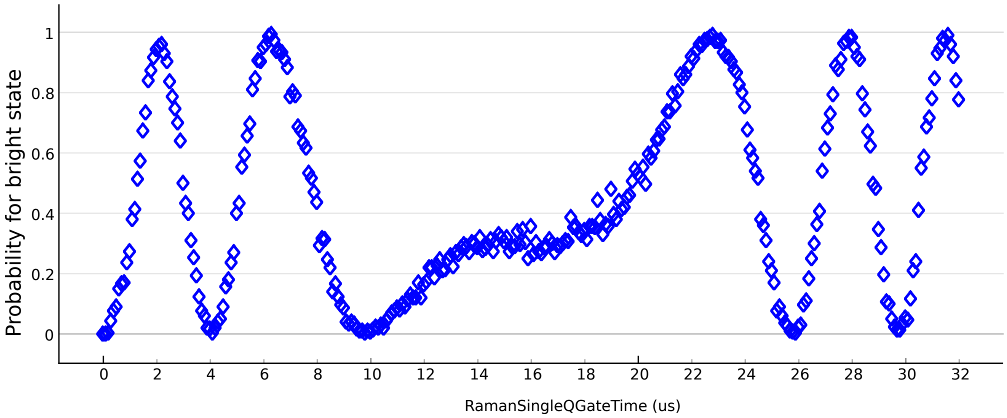

Figure 12. Timescan of BB1 compensated multi gate sequence. The probability of finding the ion in the state $|1\rangle$ is plotted for a sequence of 5 BB1 compensated $\pi/2$ pulses. We still obtain a vanishing slope at the correct gate time. However, the probability is about 30%, lower than the expected 50%. This can be caused if the $\pi/2$, π, and 2π pulses of the BB1 pulse sequence have a timing offset.

We have used gate set tomography (GST) as developed by Robin Blume-Kohout et al. at Sandia [8, 7] to characterize, calibrate and certify these single qubit operations.

We use three basic gates to implement all single qubit gates. These are G_I, the idle or identity gate, G_X, a $\pi/2$ rotation around σ_x, and G_Y, a $\pi/2$ rotation around σ_y. We prepare the qubit in the initial state $\rho \approx |0\rangle\langle 0|$ and detect the quantum state in the z-basis. GST treats the system as a black box supporting initialization, the gates G_I, G_X, G_Y and state detection. It then establishes the operations of these primitives under the assumption that the system operates in the single qubit Hilbert space and gate operations are stationary and Markovian. GST will self-consistently determine the operations up to an unobservable “gauge”. Furthermore, GST can determine whether the aforementioned assumptions are fulfilled and characterize the degree of violation of these assumptions.

Improvement of the fidelity of single qubit microwave gates

Guided by the GST analysis [8, 7] we improved the experimental setup over 5 experimental runs. Changes included the improvement of the experimental apparatus. The biggest problem identified by GST was that the gates were highly non-Markovian. Therefore, we improved the passive sta-

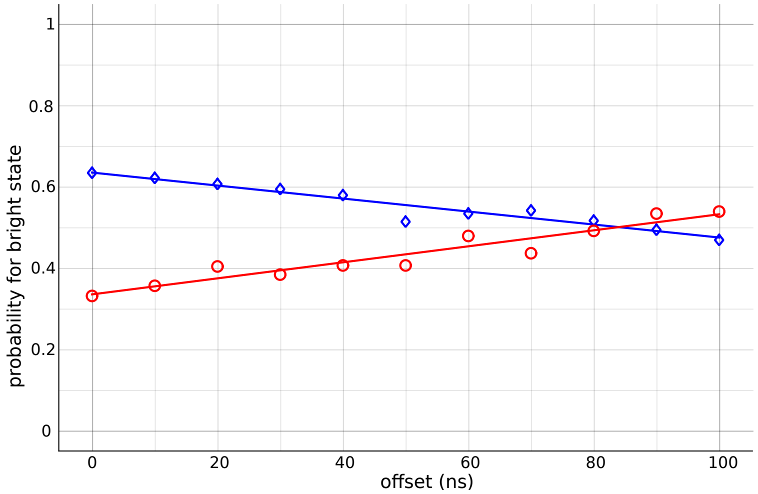

Figure 13. Calibration of BB1 pulse offset time. The probability of finding the ion in state $|1\rangle$ depends on the precise timing of the constituent pulses of the BB1 pulse sequence. Plotted is the $P(|1\rangle)$ as a function of a time offset added to all 4 constituent pulses for 101 (blue) and 103 (red) repetitions of the pulse sequence. Both cross at 50% for a offset time of 85 ns.

bility of the system by temperature stabilizing the microwave components and amplifier. We used pulse sequences to reduce dependency on the microwave amplitude (as described in section 2.3) improved the calibration of the BB1 composite pulses and developed drift control for microwave π-times and qubit resonance frequency. The implementation of the identity gate turned out to be crucial for the fidelity of all implemented gates. Because the identity gates are implemented identically for the microwave single qubit gates and laser based single qubit gates described in section 2.4, we conclude that the reason for the apparently poor performance of the identity gate is actually due to changes of the duty cycle of the microwave pulses.

To characterize the effect of different implementations of the identity gate we conducted the following concurrent experiments:

“wait”: Uncompensated G_X and G_Y gates, G_I is implemented as a wait for one π-time $T\pi$. (See Appendix A.1 for results).

“BB1 wait”: BB1 compensated G_X and G_Y gates, G_I is implemented as a wait for $4.5T_\pi$ to match the duration of the G_X and G_Y gates (where $T\pi$ denotes the π-time). (See Appendix A.2 for results).

“BB1 XX”: BB1 compensated G_X and G_Y gates, G_I is implemented as $X_\pi W_{1.25\pi}(-X)_\pi W_{1.25\pi}$ where X_π is a π rotation around σ_x and $W_{1.25\pi}$ denotes a wait time of $1.25T\pi$. (See Appendix A.3 for results).

Experimental run	Process infidelity $\times 10^3$			$1/2$ Trace distance $\times 10^3$		
	G_I	G_X	G_Y	G_I	G_X	G_Y
wait	0.02 ± 0.5	0.31 ± 0.12	0.49 ± 0.009	0.49 ± 0.53	3.0 ± 0.12	3.9 ± 0.1
BB1 wait	1.4 ± 1.2	0.19 ± 0.18	0.06 ± 0.49	4.6 ± 0.9	3.5 ± 4	2.5 ± 0.3
BB1 XX	1.2 ± 1.4	0.1 ± 0.16	0.035 ± 0.017	7.4 ± 1.8	3.6 ± 2.2	2.4 ± 0.8
BB1 XYXY	0.06 ± 0.16	0.06 ± 0.08	0.06 ± 0.04	0.07 ± 0.17	1.3 ± 1.5	1.2 ± 0.9

Table 1. Summary of the results from the microwave single qubit GST experiments.

"BB1 XYXY": BB1 compensated G_X and G_Y gates, G_I is implemented as $X_\pi Y_\pi X_\pi Y_\pi$ [25] (See Appendix A.4 for raw results).

The results of these runs are listed in Appendix A and summarized in Table 1. While the process infidelity is increased from the "wait" run to the "BB1 wait" run because the duration of all gates is increased from $T_\pi/2$ to $4.5 \times T_\pi$, the process infidelity of the G_X and G_Y gates is improved due to the reduced sensitivity of the BB1 compensated gates to amplitude fluctuations of the microwave signal. In the "BB1 wait" run, the G_I has clearly the worst fidelity. Furthermore, we believe that the larger infidelity of G_I contributes to the observed G_X infidelity due to choice of basis. If the identity gate is implemented as $X_\pi W_{1.25\pi} (-X)_\pi W_{1.25\pi}$ where X_π, the infidelity is only slightly reduced while implementing it as $X_\pi Y_\pi X_\pi Y_\pi$ reduces the infidelity of all three gates to 6×10^{-5}.

The diamond norm distance of the "BB1 XYXY" run was determined to be $< 1.9 \times 10^{-4}$. This result demonstrates that the implemented gates are above the fault tolerance threshold of 1.94×10^{-4} derived for general (coherent) noise [1].

In addition to analyzing the process and determining process infidelity, GST can assess whether the underlying assumptions, operation in a single qubit Hilbert space with stationary and Markovian operations, are fulfilled. The Markovianity violation determined by the GST algorithm as a function of sequence length is shown in Figures 14 and 15. The three plots show the same data, plotted in different ways. In Figure 15 it is clearly visible that the "wait" and "XX" implementations fo the identity gate lead to a clear violation of the assumptions below a sequence length of 100. Here, the simple "wait" performs better than the "BB1 wait" due to the 9 times shorter gate duration of uncompensated versus BB1 compensated gates. The Markovianity violation of the best "BB1 XYXY" run remains below 2σ for sequence length of up to 2048 gates. We conjecture that this is at least partially due to the constant duty cycle of microwave pulses in gate sequences using the $X_\pi Y_\pi X_\pi Y_\pi$ implementation of the identity gate.

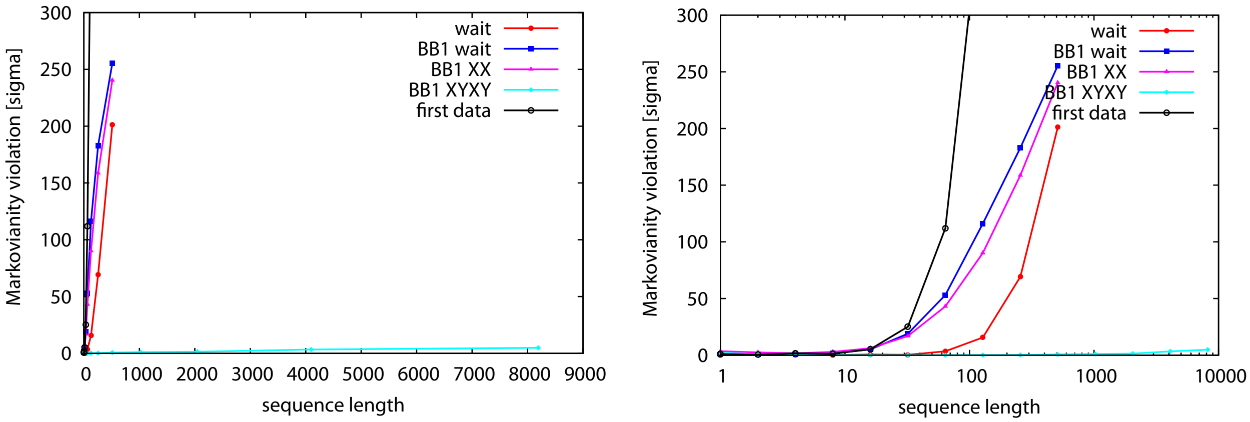

Figure 14. The Markovianity violation is shown as a function of sequence length. In linear (left) and logarithmic (right) scale as given by the GST procedure. Gates were implemented as direct gates with wait identity (red, "wait"), using broadband (BB1) compensated pulses and wait identity (blue, "BB1 wait"), using BB1 compensated pulses and the identity gates realized as $X_\pi W_{1.25\pi}(-X)_\pi W_{1.25\pi}$ (magenta "BB1 XX"), BB1 compensated pulses with $X_\pi Y_\pi X_\pi Y_\pi$ implementation of the identity gate (cyan "BB1 XYXY"). Also plotted is data from an earlier experimental run using direct gates with wait identity (black, "first data").

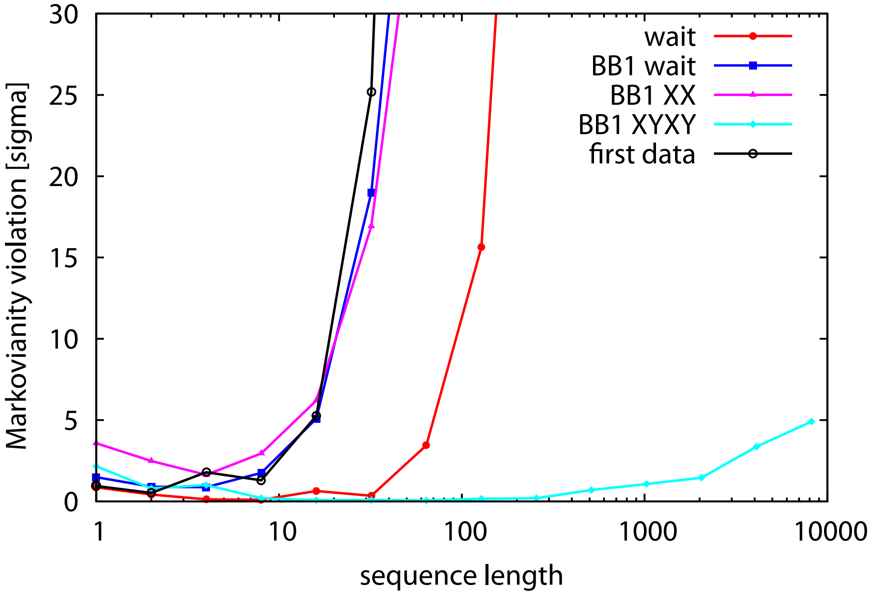

Figure 15. Detail of the data shown in Figure 14. The progress in reducing non-Markovian noise in the system is clearly visible. The best implementation, using BB1 compensated gate pulses and the identity gate implemented as $X_\pi Y_\pi X_\pi Y_\pi$, achieves a Markovianity violation of about one sigma up to a sequence length of 2048 gates.

2.4 Single qubit laser gates

Implementation of single qubit laser gates

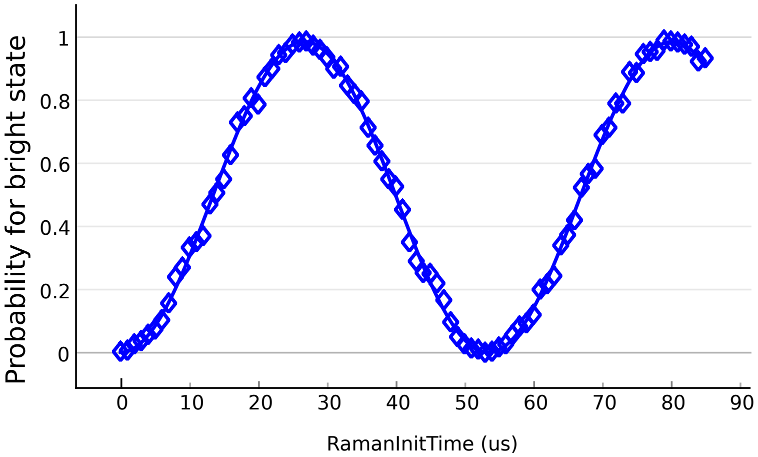

Figure 16. Copropagating Raman Rabi flopping. A single ion is exposed to two co-propagating copies of the frequency comb. Plotted is the probability to find the ion in the $|1\rangle$ state as a function of pulse duration. If the beatnote of the combs is resonant with the qubit transition, Rabi oscillations are observed.

Laser-based gates are capable of addressing single qubits in a chain, however, this comes at the cost of increased challenges in controlling fluctuations in the beam pointing, frequency, and power. While laser-based gates pose a technical challenge, the problems are not insurmountable and careful engineering of the interaction with the laser enables high-fidelity quantum operations.

Qubit operations are driven using stimulated Raman transitions, a two-photon process that requires two optical fields with a relative detuning equal to the qubit frequency $\nu_{\text{qubit}} = 12.6\,\text{GHz}$. For coherent qubit manipulations these two optical fields have to be phase stable. The necessary coherence can be easily achieved by using a pulsed laser as a source for the Raman fields. A picosecond pulsed laser has sufficient bandwidth to cover both transitions. In addition, only the relative frequency and phase of different lines of the frequency comb have to be stabilized. The laser center frequency itself is allowed to fluctuate. The frequency comb naturally provides a separation between individual comb lines that is given by the repetition rate of the laser ($\approx 118\,\text{MHz}$ for the $355\,\text{nm}$ pulsed laser used in this experiment). Comb lines separated by about 111 repetition rates can then be shifted to match the qubit frequency of the ion using acousto-optic modulators (AOMs). To control the momentum transfer on the ion, the two beams are either directed from one direction (co-propagating) or from two opposite directions (counter-propagating). Passing one of the beams through an acousto-optic modulator (AOM) allows for fine tuning of the relative offset between the two combs. Variations in the repetition rate, f_{rep}, lead to shifts in the frequency separation between relevant comb teeth. By monitoring the repetition rate directly with a phase-locked

Experimental Parameters				Infidelity $\times 10^4$		Trace Distance $\times 10^3$	
Beam Orientation	Drift Control	Compensated Gates	Gapless	Gi	max(Gx,Gy)	Gi	max(Gx,Gy)
$\Rightarrow$				0.16	11	1.3	7.1
$\Rightarrow$	✓			0.14	7.3	1.3	6.6
$\Rightarrow$		Gi, Gx, Gy		16.2	1.7	27	3.0
$\Rightarrow$	✓	Gi, Gx, Gy		10.5	2.0	15	4.0
$\Rightarrow$	✓	Gx, Gy		0.05	1.7	1.2	4.0
$\Rightarrow$	✓	Gi, Gx, Gy	✓	1.28	0.5	0.49	2.6
$\rightleftharpoons$		Gi, Gx, Gy	✓	11.1	4.1	2.3	2.7
$\rightleftharpoons$		Gx, Gy	$\checkmark^*$	0.89	5.8	8.8	2.3

Table 2. Summary of GST results for laser-based gates. Beam orientations are indicated by $\Rightarrow$ for co-propagating Raman beams and $\rightleftharpoons$ for counter-propagating Raman beams. Gapless pulses all use power-stabilized Raman beams. The gapless measurement with uncompensated I gates, marked by $\checkmark^*$, is not strictly gapless, but the only gaps occur during the wait I gates. Trace distances for max(Gx,Gy) correspond to the X or Y gate with the largest infidelity, not the maximum trace distance.

loop (PLL), we are able to detect drifts in f_{rep} and compensate for any resulting frequency and phase errors by modulating the frequency of the second Raman beam.

Because these qubit transitions are two-photon processes, an additional degree of freedom comes with the relative orientation of the two beams. If the beams are counter-propagating, Doppler shifts from center-of-mass motion of the ion will be blue-detuned for one beam and red-detuned for the other, effectively shifting the Raman transition out of resonance. This makes the transition sensitive to the motion of the ion and also allows one to change the motion of the ion. The Mølmer-Sørenson gate, however, relies on this effect to mediate the two-qubit gate operation and thus non-co-propagating beams are a necessity. Co-propagating beams are robust against temperature fluctuations in the qubit because Doppler shifts contribute to both beams equally and the relative detuning between the Raman beams remains fixed, thus giving them an advantage for single-qubit gates. This configuration also allows the frequency modulations to be applied on the same AOM and removes errors associated with propagation delays between Raman beams. For these reasons, co-propagating beams provide a great testbed for eliminating a variety of technical issues in a simplified framework that circumvents some of the difficulties associated with a counter-propagating configuration.

The natural first step is to perform GST measurements using simple gates without any compensated pulses. Although most of the work done in this first stage was used to debug experimental issues, we eventually reached a process infidelity of $\leq 1.462 \times 10^{-3}$ for the G_X and G_Y gates and a process infidelity on the order of 10^{-6} for the G_I gate (see Table 2 for a comparison of results).

These results are promising, as they reflect the natural stability of our experiment without the need for pulse compensation or frequent recalibration to account for slight deviations our gate operations. It is evident that some measures need to be taken to reduce errors in the rotation of the Bloch vector. The rotation angle depends on the Rabi frequency, which tends to vary slowly over time. Correcting for slow drifts by monitoring changes in the Rabi frequency over the course of a GST measurement reduces the infidelity down to a level of $\leq 9.16 \times 10^{-4}$. This technique cannot account for shot-to-shot fluctuations occurring on a much faster time scale.

Fluctuations of the rotation angle that are slower than individual gate pulses can be reduced by using compensated pulses. BB1 pulses have been designed to suppress amplitude errors of the driving fields to first order. Applying BB1 compensated pulses instead of un-compensated gates yields infidelities of $\leq 2.04 \times 10^{-4}$. It is important to note that for all of these data, only simple "wait" gates were used for the identity and in each case the infidelity of the I gates are $\leq 5 \times 10^{-6}$. We can only conjecture that this is because the co-propagating beams are relatively immune to thermal effects. Applying compensated G_I gates, i.e. $X_\pi Y_\pi X_\pi Y_\pi$ pulses as done with microwave gates, we get the same infidelities on the G_X and G_Y gates of $\leq 2.2 \times 10^{-4}$ but instead get an infidelity of 1.7×10^{-3} for the G_I gate This increased infidelity can be compared with the $\leq 9.16 \times 10^{-4}$ values obtained from the X and Y gates with the slow drift correction, which, for the compensated I gate, have twice the duration. At the very least, it's clear that the operations are more or less orthogonal and the difference in the I gate has little effect on the fidelities obtained for the X and Y gates.

While compensated pulses go a long way to reducing infidelities, they are not a perfect solution. One benefit of pulse compensation is that the AOMs used for applying pulses have a more consistent duty cycle when compensated G_I gates are used, particularly for sequences containing long, continuous sequences of G_I gate operations. When pulses are continuously applied, thermal drift in the AOMs is reduced and the beam intensities are more stable. Thermal drift still occurs during Doppler cooling between experiments. Leaving the Raman beams on during cooling certainly diminishes thermal drift, but power fluctuations on the 1% level are inevitable during gate sequences. Raman beam intensities can be stabilized by feeding back on the power applied to the AOM using a voltage variable attenuator (VVA). The power feedback loop response time, turn-on time of the AOM, as well as effectively discontinuous changes in the power between pulses all pose technical limitations on the feedback stability. Our solution to these problems is to use a "zero-gap" pulse sequence, in which the RF signal applied to the AOM is run in a continuous wave (CW) mode and the phase of the RF is changed for each gate operation. A zero-gap gate sequence has the benefit of providing constant power to the AOM, allowing for an extremely stable servo. Incorporating the zero-gap gate sequence does require compensated G_I gates for optimal power control, but gives a process infidelity of $\leq 7.2 \times 10^{-5}$ for G_X and G_Y gates and 1.28×10^{-4} for the compensated G_I gate.

Temperature sensitivity of the counter-propagating Raman gates adversely affects fidelity. Initial attempts at uncompensated gates without any power stabilization or gate time correction gave infidelities of $\leq 8.7 \times 10^{-3}$ for G_X and G_Y gates and 3.7×10^{-4} for the G_I gate. When the zero-gap sequence was applied, but using an uncompensated G_I gate, the infidelities of the G_X and G_Y gates dropped to $\leq 4.91 \times 10^{-4}$ but remained at 3.7×10^{-4} for the G_I gate. Because of the non-zero-gaps required for the uncompensated G_I gate, the power stabilization was not as consistent. Using $X_\pi Y_\pi X_\pi Y_\pi Y_\pi X_\pi Y_\pi X_\pi$ compensated G_I gates proved to be more reproducible for the counter-propagating Raman beams, and had infidelities of $\leq 4.22 \times 10^{-4}$ for G_X and G_Y gates and 1.16×10^{-3} for the I gate. The power stabilization with a purely zero-gap sequence does help for the G_X and G_Y gates, although the I gate is still worse when using a compensated pulse sequence.

2.5 Manipulation of the motional state of a trapped ion

Multi-qubit gates in trapped-ion systems use the strongly coupled motion of two or more ions in a trap as a quantum bus. Therefore, to realize multi-qubit gates it is necessary to address the motion of ions in the trap. In the ytterbium system the best established way to address the motion of ions in the trap is by using Raman transitions.

Resolved sideband cooling

A summary of laser cooling in trapped-ion systems can be found in [14]. Doppler cooling is usually not sufficient to cool a trapped ion to its motional ground state. The original Cirac-Zoller [11] gate requires the ions to be in the motional ground state. While the Mølmer-Sørensen gate does not have this requirement [48], it is still beneficial to cool the ion to the motional ground state to improve the gate fidelity. For resolved sideband cooling (see Figure 17) the quantum state of the harmonic oscillator has to be addressed by Raman transitions. The ion has to be excited from $|0\rangle$ to $|1\rangle$ while removing a motional quantum. The ion is then pumped back from $|1\rangle$ to $|0\rangle$ before the Raman transition is repeated. If the population has accumulated in the ground state of the motion, the quantum number cannot be further reduced and the transition from $|0,n\rangle \rightarrow |1,n-1\rangle$ cannot be induced any more.

The Rabi frequency of the motion extracting transition is

$$\Omega_{n,n-1} \approx \eta \Omega \sqrt{n}, \tag{4}$$

while the Rabi frequency on the motion adding sideband is

$$\Omega_{n,n+1} \approx \eta \Omega \sqrt{n+1}, \tag{5}$$

where Ω is the carrier Rabi frequency and η is the Lamb-Dicke parameter. The dependency of the Rabi frequency on the motional state leads to a dephasing of the Rabi oscillations for different motional states as can be seen for the sideband Rabi flopping signals of the Doppler cooled ion in Figure 18 (open symbols). After ground state cooling, the motion extracting (red) sideband cannot be driven any more and the motion adding (blue) sideband has a well-defined Rabi frequency that is smaller than the Rabi frequency of the Doppler cooled ion.

In addition, the Rabi frequency of the carrier transition, which does not change the motion of the ion, also depends on the motional state:

$$\Omega_{n,n} = \Omega e^{-\eta^2/2} L_n(\eta^2), \tag{6}$$

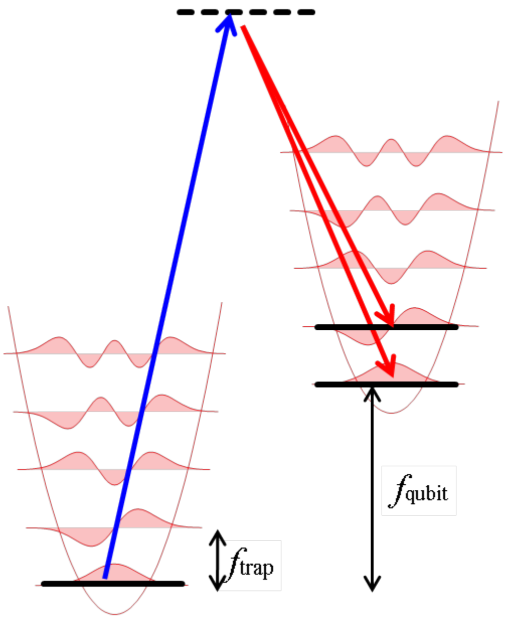

Figure 17. Schematic detailing Raman sideband cooling of trapped ions. Each of the two hyperfine qubit states has a ladder of harmonic oscillator states. Raman transitions between the qubit states can address the motion of the ion. Resolved by the laser frequency, transitions that maintain the motional quantum state (carrier transition) or increase (reduce) the motional quantum number by one (red, blue motional sideband) can be realized. If this transition is driven on the red sideband, one motional quantum is extracted. A subsequent state initialization pulse reinitializes the ion in $|0\rangle$. Repeating this procedure implements resolved sideband cooling.

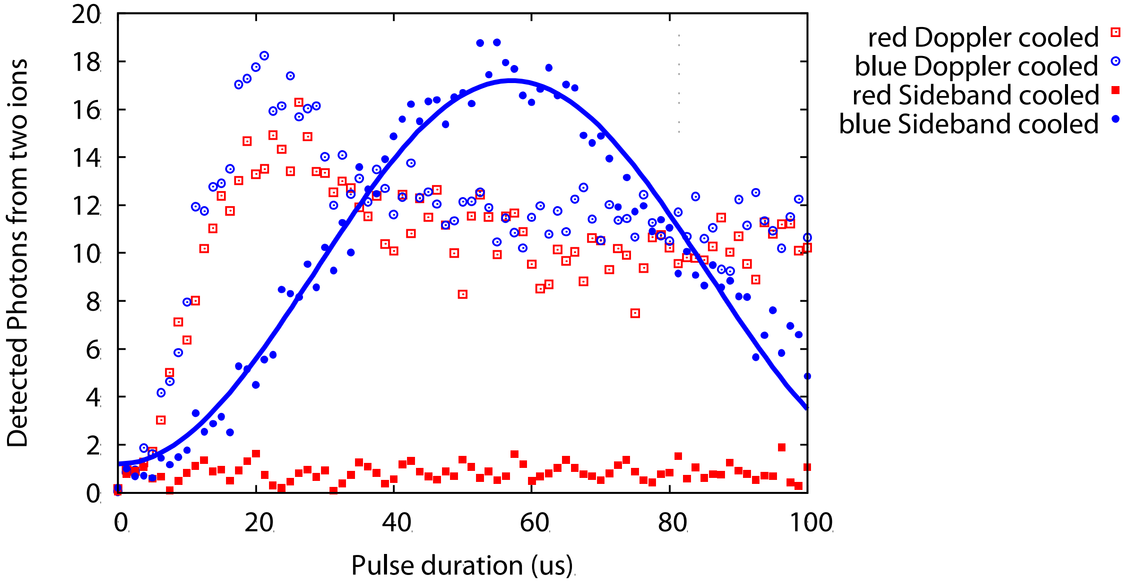

Figure 18. Demonstration of sideband cooling near the motional ground state. Population of the $|1\rangle$ state is depicted as a function of pulse duration. Rabi flopping on the blue and red motional sideband (blue and red data, respectively) is shown for a Doppler cooled ion (open symbols), and a sideband cooled ion (solid symbols). If the ion is in the motional ground state, the red sideband cannot be driven because there is no target state. The residual faster oscillation that is visible in the data is from off-resonant transitions on un-cooled modes. The π-time of the transition is proportional to $\frac{1}{\sqrt{n}}$ where n is the quantum number of the harmonic oscillator.

where $\Omega = \Omega_{0,0}$ is the ground state carrier Rabi frequency, η is the Lamb-Dicke parameter and L_n is the nth Laguerre polynomial. The de-phasing of the Rabi frequencies for different motional states can be seen in a motion sensitive Rabi carrier oscillations of Figure 19. The decay of the carrier Rabi oscillation can therefore also be used for to measure the temperature of a trapped ion [47].

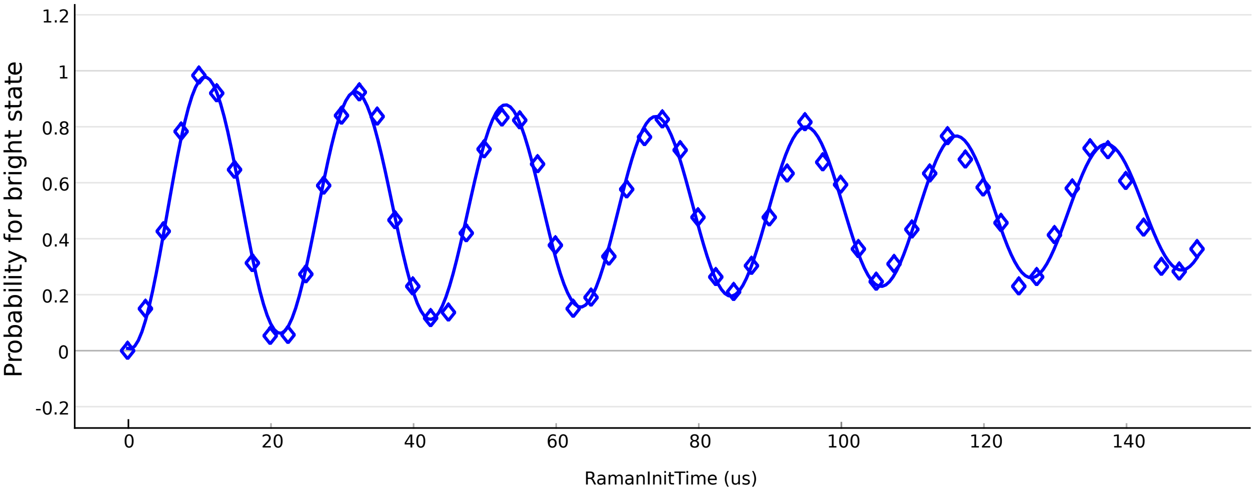

Figure 19. Raman Rabi flopping using motionally sensitive counter-propagating Raman beams. In this configuration the π-time is a function of the quantum number of the harmonic oscillator. The different quantum numbers in a thermal ensemble lead to the observed damping of the Rabi oscillations.

Characterization of trap heating rates

Heating of the ion's motion [10] during multi-qubit gates will limit the fidelity of the multi-qubit operation. Heating in ion traps is usually higher than expected from the Johnson noise of the voltage on the trap electrodes. Therefore, a precise characterization of the heating rates of a trap is important to achieve good multi-qubit gate fidelities. Cryogenic cooling [27], argon ion milling [23] and laser treatment [2] have been shown to reduce heating rates in surface electrode ion traps.

Here we characterized the heating rates of a two-ion crystal in the Thunderbird trap and of a single ion in the HOA-2 trap. The 6 degrees of freedom of two ions lead to 6 normal modes of motion. These are (Figure 20) the longitudinal center of mass and stretch modes, and the transversal center of mass and tilt mode. Because there are two orthogonal transversal directions the transversal center of mass and tilt mode have two modes each.

The transversal center of mass modes are sensitive to voltage noise at the location of the ions, while the transversal tilt modes are only sensitive to voltage gradient noise at the location of the

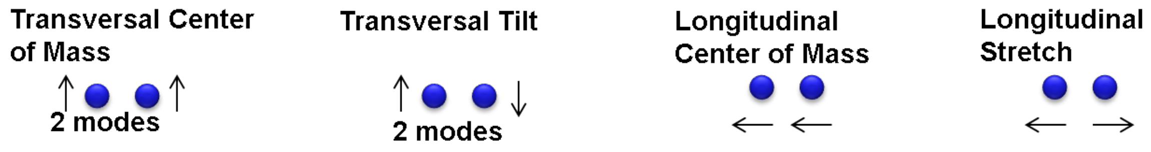

Figure 20. Normal modes in a two-ion chain. There a 6 normal modes. There are two transversal center of mass modes in the two orthogonal transversal directions and two transversal tilt modes. The two longitudinal modes are the center of mass mode and the stretch mode.

ions. Therefore, we expect the tilt modes to show considerably lower heating rates than the center of mass modes. Heating rates for the two-ion center of mass modes in the Thunderbird trap are shown in Figure 21. We measured heating rates of 0.4 quanta/ms and 1.7 quanta/ms for the 1.94 MHz and 2.38 MHz modes, respectively.

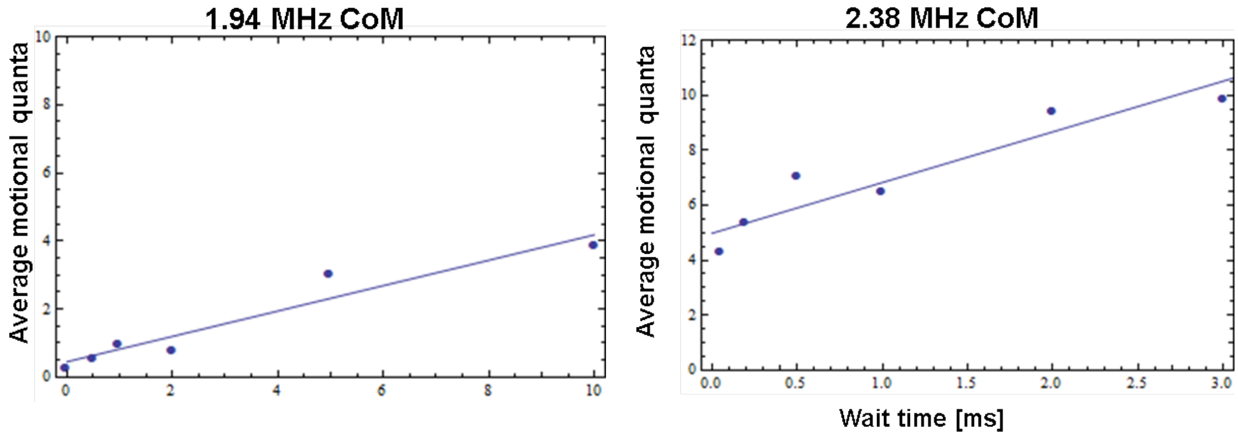

Figure 21. Heating rates on the Thunderbird center of mass modes. Average motional quanta as a function of the wait time between sideband cooling and thermometry. The heating rate is determined by a linear fit. The heating rate of the 1.94 MHz mode is ≈ 0.4 quanta/ms, the 2.38 MHz mode was heated with a rate of ≈ 1.7 quanta/ms.

The heating rates of the two-ion tilt modes in the Thunderbird trap are shown in Figure 22. Here we only observe heating rates below ≈ 1 quanta/s and 8 quanta/s for the modes at 1.84 MHz and 2.32 MHz, respectively.

Due to the lower heating rates, we used the transversal tilt modes to realize the two-qubit gate. In the HOA-2 trap we have observed lower heating rates than in the Thunderbird trap. For the

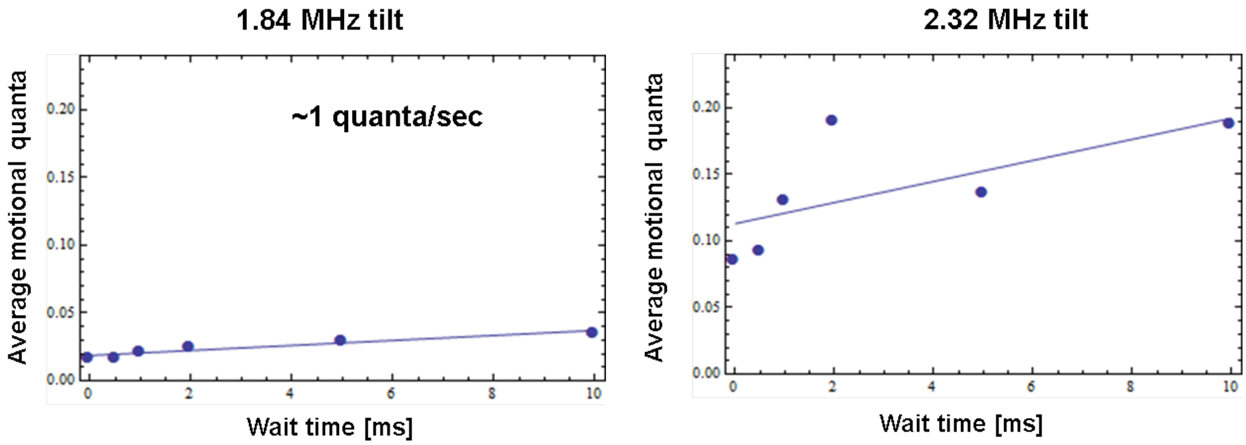

Figure 22. Heating rates for the Thunderbird tilt modes. Fluctuating fields that are common mode with respect to the two ions cannot excite the tilt modes. To heat the tilt mode a fluctuating electric field gradient at the location of the ion chain is necessary. This can be seen from the measured heating rates. For the 1.84 MHz tilt mode the heating rate is $< 1\,\mathrm{quant/s}$ while the 2.32 MHz tilt mode heats be $< 8\,{}^{\mathrm{quanta}}\!/\!{}_{\mathrm{s}}$. Thus the heating rates of the tilt modes are at least a factor of 100 smaller than the center of mass modes.

single ion mode for a principal axis parallel to the trap surface we have observed a heating rate of about $40\,{}^{\mathrm{quanta}}\!/\!{}_{\mathrm{s}}$. This heating rate was independent of the location of in the central slotted section of the HOA-2 trap (see Figure 23).

We have also measured the heating rate as a function of the principal axes rotation (Figure 24). Here, we see that the heating rate is lowest if the normal mode axis is parallel to the trap surface (rotation gain 0) and increases by a factor of about 2.3 for the maximal characterize angle of about 40°. This corresponds to an anisotropy of about 5 between the axis parallel and perpendicular to the trap surface. All established theories for the intrinsic trap heating rates predict anisotropies of ≤ 2 [44]. This leads to the conclusion that the heating rates in directions that are not parallel to the trap surface are limited by technical noise.

2.6 Two-qubit gate realization

Mølmer-Sørensen interaction

A realization of a two-qubit gate that does not require ground state cooling was proposed by Mølmer and Sørensen in 1999 [48, 49]. A detailed description on the implementation of this gate using pulsed lasers in the ytterbium system was described by Hayes [21].

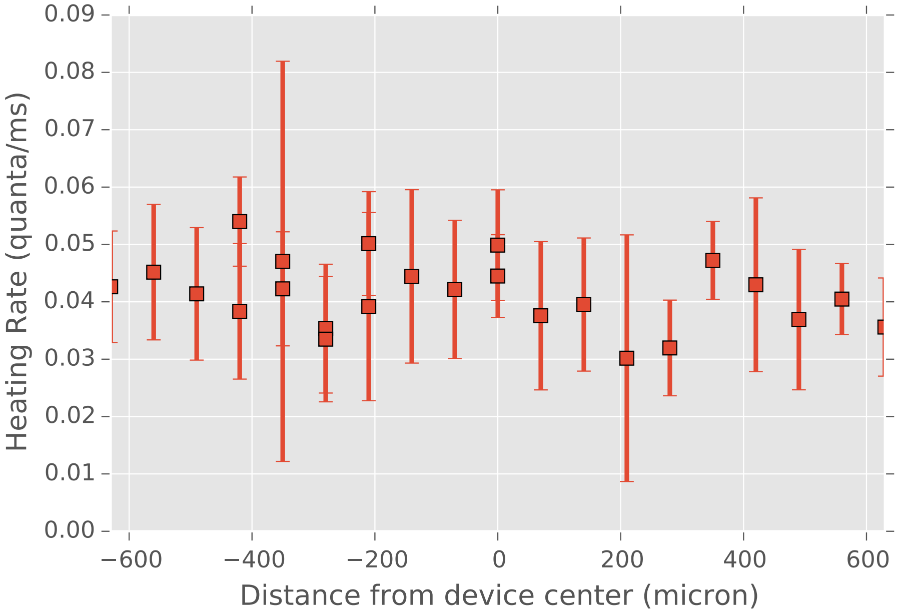

Figure 23. Heating rates of the HOA-2 trap. The heating rate for the 2.8 MHz radial mode was measured to be about 40 quanta/s. The heating rate does not vary along the trap.

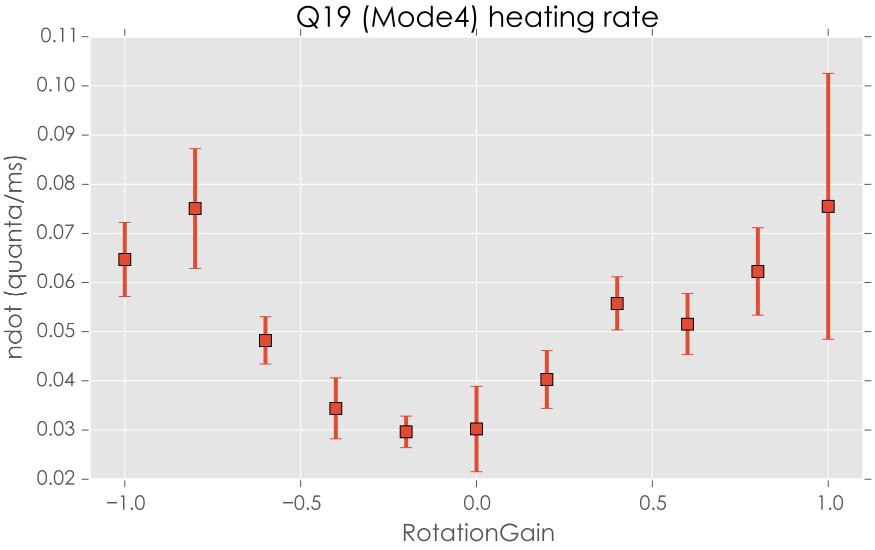

Figure 24. Heating rates as function of principal axes rotation fro HOA-2 trap. The heating rate is minimal if the mode axis is aligned parallel to the trap surface. The heating rate increases as the mode is tilted. For a rotation gain of 1 we expect a principal axes rotation angle of about 40°.

The two-qubit gate is mediated by the motion of the ions and relies on a spin-dependent force due to which different spin-states trace different paths on phase space. However, in order to disentangle spin-states and motion at the end of the gate operation, the initial and final phase space distributions have to overlap. The higher excited the motion of the mode used for this gate, the more precise the classical control has to be to achieve sufficient overlap. Hayes et al. [19] developed a scheme for coherent error suppression for these gates that was used in all experiments described here.

The two-qubit gate induced by Raman lasers can be realized in a way that is sensitive to the optical phase of the Raman beams and a way insensitive to the optical phase of the Raman beams [24]. The phase sensitive configuration is realized if the Δk_1 and Δk_2 of the bichromatic field inducing the Mølmer and Sørensen gate are parallel. The phase insensitive configuration is reached if they are anti-parallel. While the phase-insensitive configuration has several advantages,

- increased stability and higher fidelity
- can be combined with global microwave gates
- motion insensitive single qubit gate can be used,

the gate realized in this work is the phase sensitive version of the gate.

2.7 Two-qubit gate characterization

The basic gate operation of the Mølmer and Sørensen gate is

$$|00\rangle \rightarrow |00\rangle + |11\rangle \tag{7}$$

To demonstrate that this operation is realized one has to show that the population after the gate operation was applied to a $|00\rangle$ state is $|00\rangle + |11\rangle$. In addition it has to be shown that this is a coherent superposition rather than a mixed state. In Figure 25, a scan of the detuning of the bichromatic field from the motional mode is shown. For the correct gate detuning of $-13\,\text{kHz}$ the probability of detecting one bright ion (red) vanishes while zero and two bright ions are each found with 50% probability.

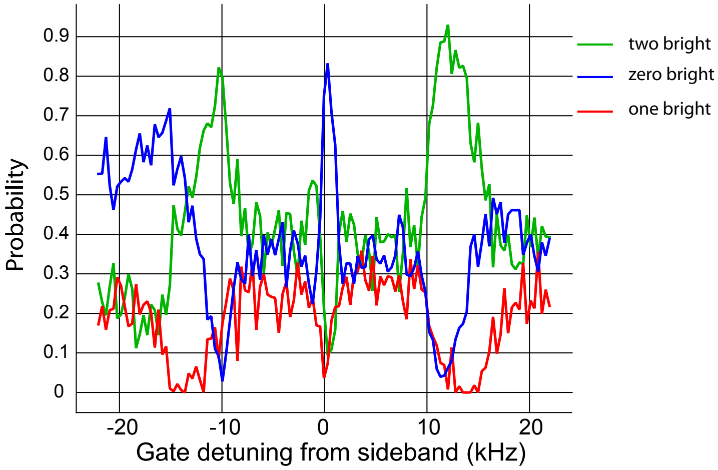

Figure 25. The Mølmer-Sørensen operation applied to the $|00\rangle$ state as a function of the detuning of the bichromatic field from the motional modes. For a detuning of $-13\,\text{kHz}$ a Mølmer Sørensen gate is realized. This can be seen because the probability of detecting one bright ion (red) vanishes while zero and two bright ions are each found with 50% probability.

To prove the coherence of the generated entangled state, a measurement of the off-diagonal elements of the density matrix is necessary. This can be achieved by a $\pi/2$ pulse on both ions with an adjustable phase (see Figure 26). Depending on the phase, the final state can then reach the maximum $|00\rangle + |11\rangle$ and minimum $|01\rangle = |1\rangle\rangle$ of parity. Here the parity is defined as

$$\mathscr{P} = P(|11\rangle) + P(|00\rangle) - P(|01\rangle) - P(|10\rangle). \tag{8}$$

The contrast of the parity oscillations as a function of the phase of the analysis $\pi/2$ pulse, together with the populations measure after the gate, yields the fidelity of the entangled state

$$\mathscr{F} = \frac{1}{2}\left(P(|00\rangle) + P(|11\rangle)\right) + \frac{1}{4}\mathscr{P}. \tag{9}$$

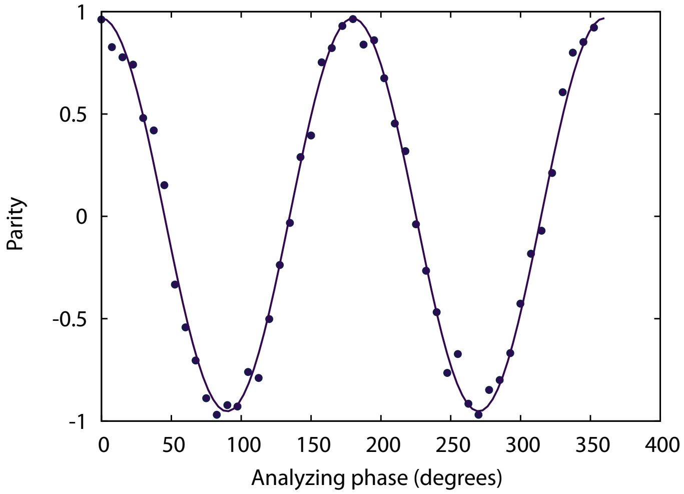

Figure 26. The Mølmer-Sørensen gate is followed by a single qubit $\pi/2$ pulse with adjustable phase. The parity $P(|11\rangle) + P(|00\rangle) - P(|10\rangle) - P(|01\rangle)$ is plotted as a function of the phase of the analyzing pulse.

The data shown in Figure 25 and Figure 26 yields a entanglement fidelity of 97.7%. This is the highest entanglement fidelity reported for any two-qubit gate in a microfabricated surface trap.

3 Quantum algorithms for our quantum information processor

In parallel to the experimental development of our trapped-ion two-qubit quantum information processor, we investigated quantum algorithms that might be able to leverage quantum information systems with a relatively small number of qubits to solve problems with potential mission interest. In particular we focused on graph and discrete-optimization problems, which are able to capture a wide variety of practical applications. Developing quantum algorithms with a provable performance improvement over their classical counterparts has proven a daunting task. In the 20 years since Shor's groundbreaking quantum algorithm for integer factoring [46], only a handful of new quantum algorithms, generally providing very modest advantages, have been invented. Thus our algorithmic goal for this LDRD was to evaluate existing quantum algorithms rather than attempt to develop new ones, and adapt them as necessary in the context of our experimental work.

We highlight three of our efforts here. Our first was to develop a general theoretical quantum gate model based on Mølmer-Sørensen gate that our trapped-ion system realizes. Next, we suggest a very simple algorithm implementable on a two-qubit quantum system. Finally we present an alternate analysis of a recent quantum algorithm by Farhi et al. [16, 15, 15] for approximately solving discrete optimization problems using low-depth quantum circuits.

3.1 Gate model

Quantum algorithms are typically constructed from sets of gates such as the Paulis, the Hadamard, T, and the CNOT; however, once the experimental system supports individual addressing, only the single body operations $e^{-i\theta X/2}$ and $e^{-i\theta Y/2}$ and the two-qubit operation $e^{-i\frac{\pi}{4}(X cos\theta + Y sin\theta)^{\otimes 2}}$ will be natively available to the ion trap. From these native gates other more commonly used gates were determined to facilitate compiling algorithms for the system.

Euler Angles

Any single qubit gate may be composed using Euler angle rotations and a global phase, for example

$$U = e^{i\alpha} R_Z(\beta) R_X(\gamma) R_Z(\delta) = e^{i\alpha'} R_X(\beta') R_Y(\gamma') R_X(\delta'), \tag{10}$$

where any rotation about a unitary U is given by

$$R_U(\theta) = e^{-iU\theta/2}. \tag{11}$$

The system natively has the rotations $R_X(\theta)$ and $R_Y(\theta)$. Rotation about Z can be achieved as

$$R_Z(\theta) = R_X(\pi/2) R_Y(\theta) R_X(-\pi/2), \tag{12}$$

where the global phase was dropped. The global phase will be ignored in the sequel as well.

Paulis

The Paulis X and Y are simply

$$X = R_X(\pi), \tag{13}$$

and

$$Y = R_Y(\pi). \tag{14}$$

While Pauli Z could be obtained from Eq. 12, only two rotations are needed. That is, Z can be obtained by

$$Z = R_Y(\pi)R_X(\pi). \tag{15}$$

Reducing the number of gates applied to get another gate is preferable since each application of a gate will likely increase the amount of error in the system.

The Hadamard

The Hadamard is given by

$$H = R_X(\pi)R_Y(\pi/2). \tag{16}$$

The T gates

The T gate is

$$T = R_Z(\pi/4) = R_X(\pi/2)R_Y(\pi/4)R_X(-\pi/2). \tag{17}$$

The $T^\dagger$ gate is obtained by

$$T^\dagger = R_Z(-\pi/4) = R_X(\pi/2)R_Y(-\pi/4)R_X(-\pi/2). \tag{18}$$

Two-qubit gates

The two-qubit gates most commonly employed for quantum alogirthms are the controlled-Z gate and the CNOT. These may be enacted by the Mølmer-Sørensen gate $e^{-i\pi/4\, X\otimes X}$, which will depicted as shown in Figure 27.

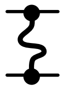

Figure 27. The Mølmer-Sørensen gate $e^{-i\pi/4\, X\otimes X}$.

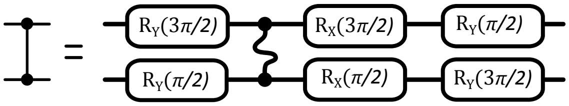

Figure 28. The controlled-Z gate.

Using the two-qubit gate $e^{-i\pi/4XX}$ and single-qubit rotations, the controlled-Z gate may be obtained as in Figure 28.

Similarly, CNOT may be formed according to Figure 29.

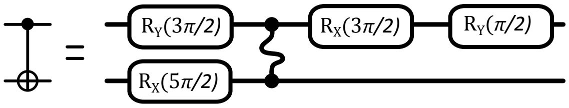

Figure 29. The CNOT gate.

Characterizing the System

Currently, the experimental two-ion system does not support individual addressing; therefore, instead of being able to apply the single-qubit gates $R_X(\theta)$ and $R_Y(\theta)$ to each ion, the gates $R_X(\theta)\otimes R_X(\theta)$ and $R_Y(\theta)\otimes R_Y(\theta)$ are applied as well as the Mølmer-Sørensen gate $e^{-i\frac{\pi}{4}(Xcos\theta+Ysin\theta)^{\otimes 2}}$. Since the gates act symmetrically, the ions are initialized in the state $|00\rangle$, and the basis states $|00\rangle$, $|11\rangle$, and $\frac{1}{\sqrt{2}}(|00\rangle+|11\rangle)$ are measured, the system stays in the symmetric subspace of two qubits.

Most quantum algorithms currently rely on systems composed of qubits; however, the two ion system without individual addressing may be treated as a qutrit with basis states $|0\rangle=|00\rangle$, $|1\rangle=|11\rangle$, and $|2\rangle=\frac{1}{\sqrt{2}}(|00\rangle+|11\rangle)$. Characterizing the error of such a qutrit system will allow the implementation and exploration of algorithms that make use of the higher dimensional freedom of the qutrit, as well as help to characterize and reduce error in controlling the two qubits once individual addressing is made available.

In order to characterize the error in the system, one must be able to produce states that span the space. Such states can be achieve by initializing in the state $|00\rangle$ and then applying appropriate rotation resulting in the states

$$
\begin{align}
|\psi_1\rangle &= |00\rangle \tag{19}\\
|\psi_2\rangle &= R_X(3\pi/2) \otimes R_X(3\pi/2)|00\rangle \tag{20}\\
|\psi_3\rangle &= R_Y(3\pi/2) \otimes R_Y(3\pi/2)|00\rangle \tag{21}\\
|\psi_4\rangle &= R_X(\pi/2) \otimes R_X(\pi/2)|00\rangle \tag{22}\\
|\psi_5\rangle &= R_Y(\pi/2) \otimes R_Y(\pi/2)|00\rangle \tag{23}\\
|\psi_6\rangle &= R_Y(\pi) \otimes R_Y(\pi)|00\rangle \tag{24}\\
|\psi_7\rangle &= M|00\rangle \tag{25}\\
|\psi_8\rangle &= R_X(\pi/2) \otimes R_X(\pi/2)\, M|00\rangle \tag{26}\\
|\psi_9\rangle &= R_Y(\pi/2) \otimes R_Y(\pi/2)\, M|00\rangle, \tag{27}
\end{align}
$$

where $M = e^{-i\pi/4\, X\otimes X}$.

Besides being able to fully span the space, in order to characterize the system one must also be able to make measurements that collapse the space onto a set of vectors that span the space. This can be achieve by measuring the following unitaries:

$$
\begin{align}
U_1 &= I \tag{28}\\
U_2 &= R_X(pi/4) \otimes R_X(\pi/4) \tag{29}\\
U_3 &= R_Y(pi/2) \otimes R_Y(\pi/2) \tag{30}\\
U_4 &= R_Y(pi/4) \otimes R_Y(\pi/4) \tag{31}
\end{align}
$$

3.2 A discrete quantum walk on two qubits

The canonical discrete quantum walk consists of a pointer space and a coin space [52]. The pointer indicates the position of the walker, while the coin determines the direction the walker moves. The pointer space is a register that represents the positive and negative integers on a number line, while the coin space is the space of a single qubit. Typically, pointer and coin are initialized to the state $|0\rangle_c|0\rangle_p$, where the subscript c indicates the coin and the subscript p indicates the pointer. The coin state is then "flipped" by applying the Hadamard gate

$$
H = \frac{1}{\sqrt{2}}\begin{pmatrix} 1 & 1 \\ 1 & -1 \end{pmatrix} \tag{32}
$$

on the coin state. The pointer is then incremented by -1 (to the left) or by +1 (to the right) depending on the state of the coin. The process of incrementing the pointer is carried out by applying the shift operator

$$
S = |0\rangle\langle 0|_c \sum_i |i+1\rangle\langle i|_p + |1\rangle\langle 1|_c \sum_i |i-1\rangle\langle i|_p. \tag{33}
$$

A single step of the quantum walk is the application of the coin flipping operation and followed by the shift operation $U = S(H_c \otimes I_p)$. The quantum discrete quantum walk is then the repeated application of the unitary U.

The experimental system we are investigating is composed of two qubits. Instead of having a system of one coin qubit and a state that can represent any positive or negative integer, we have a system consisting of two qubits. These two qubits can implement a coin and a number line of 0 and 1. In the case of a pointer that represents a finite number line, one natural modification to the canonical discrete quantum walk is to make the boundary closed. In this case, shifting to the right from the state $|1\rangle_p$ leads to the state $|0\rangle_p$ and shifting to the left from the state $|0\rangle_p$ leads to the state $|1\rangle_p$. This results in a new shift operator

$$\begin{aligned} S' = \; & |0\rangle\langle 0|_c(|0\rangle\langle 1|_p + |1\rangle\langle 0|_p) + \\ & |1\rangle\langle 1|_c(|0\rangle\langle 1|_p + |1\rangle\langle 0|_p). \end{aligned} \tag{34}$$

This is equivalent to the shift operation

$$S' = I_c X_p. \tag{35}$$

The overall quantum walk operation then becomes

$$U' = H_c X_p, \tag{36}$$

which does not allow the two qubits to interact and, therefore, is not very interesting. To make the quantum walk less trivial, we can modify the shifter operator so that the shift is only applied if the coin is in the $|1\rangle_c$ state. This results in the shift operation

$$S'' = |0\rangle\langle 0|_c I_p + |1\rangle\langle 1|_c X_p = CNOT_{c,p}. \tag{37}$$

A single quantum walk operation then becomes

$$U'' = CNOT_{c,p}(H_c \otimes I_p), \tag{38}$$

Eq. 38 can then be realized by the circuit in Figure 30, which is composed of gates native to ion traps.

Depending on numbers of steps using Eq. 38, measurement results of the pointer state will show a 100% probability of the pointer being in state $|0\rangle$, 100% probability of the pointer being in state $|1\rangle$, or a 50% probability of the pointer being in state $|1\rangle$ or state $|1\rangle$. While this does not directly follow the probability distribution of the canonical quantum walk, the quantum walk using Eq. 38 provides the first steps moving towards a full-fledged quantum walk, which would require more qubits. Further, this modification of the quantum walk is useful experimentally, since with certain numbers of steps the pointer should be found, for example, in state $|1\rangle$ with 100% probability. Deviation away from 100% would only be the result of experimental error. Thus, this quantum walk can be used to explore experimental error on algorithms.

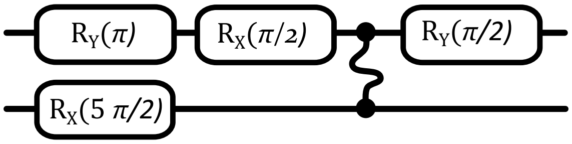

Figure 30. The gate U'' where the top line represent the clock qubit and the bottom line represents the pointer qubit.

3.3 The Quantum Approximate Optimization Algorithm

For hard discrete optimization problems, efficient algorithms that always deliver an exact solution may not be viable. A natural approach for such problems is to design an efficient algorithm that produces an approximately optimal solution instead of an exactly optimal solution. Moreover, for many mission-relelvant applications, one seeks to know the quality of a generated approximate solution relative to the optimal solution quality. Approximation algorithms provide such a guarantee.

Although classical approximation algorithms for a great many graph-analysis and discrete-optimization algorithms have been known for decades, the very first quantum approximation algorithms were only recently developed by Farhi et al. [16, 15]. They do so within the context of a framework they call the Quantum Approximation Optimization Algorithm (QAOA). They were able to achieve a victory for quantum algorithms in producing a quantum approximation algorithm for a variant of the well-known boolean satisfiability problem that was able to provably deliver a better-quality approximate solution than the best known classical algorithm at the time, which was 15 years old [15]. However, soon after this result was published, a team of classical algorithms experts discovered a new classical algorithm that achieved what is believed to be the best possible quality guarantee, beating that of the QAOA-based quantum algorithm [5]. In a final stroke, Farhi et al. improved their analysis to show that it also indeed achieved the same guarantee as the classical algorithm [15].

We were interested in the QAOA algorithm because it provides a simple and natural quantum strategy for solving hard discrete-optimization problems. A quantum-circuit implementation of QAOA requires low depth, which is desirable from an experimental perspective. Soon after the initial QAOA-based approximation algorithms were published, we sought to better understand the framework. In the process we drafted a more complete and rigorous proof of the initial performance guarantee of QAOA on bounded-occurrence satisfiability problems. For completeness, we include our alternate analysis below. The analysis below follows much of Farhi et al.'s original analysis and assumes familiarity with their work [15].

An instance of Max-E3-LIN2 consists of m constraints over the variables, $z_i \in \{-1,1\}$ for $1 \leq i \leq n$:

$$z_i z_j z_k = b_{ijk} \text{ for } \{i,j,k\} \in \mathscr{C},$$

where $b_{ijk} \in \{-1,1\}$. For each $\{i,j,k\} \in \mathscr{C}$ we assume that i, j, and k are distinct and that the variables z_i, z_j, and z_k appear together in at most one constraint. We seek an assignment to the variables that maximizes the number of satisfied constraints. We consider the *bounded-occurrence* version of the problem, in which each variable x_i appears in at most D constraints.

We analyze the Quantum Approximate Optimization Algorithm applied to the above problem as described by Farhi et al. [15]. We let B be a sum of σ_x operators over the variables above, $B = \sum_i X_i$, and our objective operator is $C = \sum_{\{i,j,k\}\in\mathscr{C}} \left(\frac{1}{2}I + \frac{b_{ijk}}{2} Z_i Z_j Z_k\right)$. We have that the expected number of constrains satisfied by the Quantum Approximate Optimization Algorithm is:

$$\begin{aligned}\langle s|e^{-i\gamma C}e^{i\beta B}Ce^{-i\beta B}e^{i\gamma C}|s\rangle &= \sum_{\{i,j,k\}\in\mathscr{C}} \left(\frac{1}{2} + \frac{b_{ijk}}{2}\langle s|e^{-i\gamma C}e^{i\beta B}Z_iZ_jZ_ke^{-i\beta B}e^{i\gamma C}|s\rangle\right)\\ &= \frac{m}{2} + \frac{1}{2}\sum_{\{i,j,k\}\in\mathscr{C}} b_{ijk}\langle s|e^{-i\gamma C}e^{i\beta B}Z_iZ_jZ_ke^{-i\beta B}e^{i\gamma C}|s\rangle .\end{aligned}$$

Following (9) from Farhi et al., with $\beta = \pi/4$, we have $e^{i\beta B}Z_iZ_jZ_ke^{-i\beta B} = Y_iY_jY_k$. We are interested in the expected number of constraints satisfied beyond $\frac{m}{2}$, and focus only on the second term above,

$$\frac{1}{2}\sum_{\{i,j,k\}\in\mathscr{C}} b_{ijk}\langle s|e^{-i\gamma C}Y_iY_jY_ke^{i\gamma C}|s\rangle . \tag{39}$$

As Farhi et al., we define finer-granularity operators over the terms of C involving a just single qubit u or pairs of distinct qubits u and w:

$$\begin{aligned}C_u &= \frac{1}{2}\sum_{\substack{v,w:\\ \{u,v,w\}\in\mathscr{C}}} b_{uvw}Z_vZ_w,\\ C_{uv} &= \frac{1}{2}\sum_{\substack{w:\\ \{u,v,w\}\in\mathscr{C}}} b_{uvw}Z_w, \text{ and}\\ C_{uvw} &= \frac{1}{2}b_{uvw}Z_uZ_vZ_w.\end{aligned}$$

Then for distinct qubits i, j, and k, we may collect all terms of C involving any of these qubits: $\overline{C}_{ijk} = Z_iC_i + Z_jC_j + Z_kC_k + Z_iZ_jC_{ij} + Z_iZ_kC_{ik} + Z_jZ_kC_{jk} + C_{ijk}$. Now, we may express C as $C = \frac{m}{2}I + \frac{1}{2}\sum_{\{u,v,w\}\in\mathscr{C}} b_{uvw}Z_uZ_vZ_w = \frac{m}{2}I + \widetilde{C}_{ijk} + \overline{C}_{ijk}$, where $\widetilde{C}_{ijk}$ represents all terms of C that involve none of i, j, and k.

Our analysis diverges slightly from that of Farhi et al. at this point. Returning to (39), we have:

$$\begin{aligned}&\frac{1}{2}\sum_{\{i,j,k\}\in\mathscr{C}} b_{ijk}\langle s|e^{-i\gamma C}Y_iY_jY_ke^{i\gamma C}|s\rangle\\ =&\frac{1}{2}\sum_{\{i,j,k\}\in\mathscr{C}} b_{ijk}\langle s|e^{-i\gamma(\frac{m}{2}I+\widetilde{C}_{ijk}+\overline{C}_{ijk})}Y_iY_jY_ke^{i\gamma(\frac{m}{2}I+\widetilde{C}_{ijk}+\overline{C}_{ijk})}|s\rangle\\ =&\frac{1}{2}\sum_{\{i,j,k\}\in\mathscr{C}} b_{ijk}\langle s|e^{-i\gamma\overline{C}_{ijk}}Y_iY_jY_ke^{i\gamma\overline{C}_{ijk}}|s\rangle\end{aligned}$$

We will first simplify the term, $\langle s|e^{-i\gamma\overline{C}_{ijk}}Y_iY_jY_ke^{i\gamma\overline{C}_{ijk}}|s\rangle$ in the sum above for qubits i, j, and k by inserting a complete set of qubits:

$$\begin{aligned}
&\sum_{s_i,s_j,s_k} \langle s|e^{-i\gamma\overline{C}_{ijk}}Y_iY_jY_k|s_i,s_j,s_k\rangle\langle s_i,s_j,s_k|e^{i\gamma\overline{C}_{ijk}}|s\rangle \\
&= \sum_{s_i,s_j,s_k} \langle s|e^{-i\gamma\overline{C}_{ijk}}|\widetilde{s_i},\widetilde{s_j},\widetilde{s_k}\rangle - i(-1)^{s_i}(-1)^{s_j}(-1)^{s_k}\langle s_i,s_j,s_k|e^{i\gamma\overline{C}_{ijk}}|s\rangle, \qquad (40)
\end{aligned}$$

where $\widetilde{s_u} = 1 - s_u$. Letting $\bar{s} = \Pi_{q\in\{1,\dots,n\}\setminus\{i,j,k\}}|+\rangle_q$, we observe that:

$$\langle s|e^{-i\gamma\overline{C}_{ijk}}|\widetilde{s_i},\widetilde{s_j},\widetilde{s_k},\bar{s}\rangle = \langle s|e^{i\gamma\overline{C}_{ijk}}|s_i,s_j,s_k,\bar{s}\rangle.$$

Hence (40) becomes:

$$\sum_{s_i,s_j,s_k} -i(-1)^{s_i}(-1)^{s_j}(-1)^{s_k}\langle s|e^{-i\gamma\overline{C}_{ijk}}|s_i,s_j,s_k\rangle\langle s_i,s_j,s_k|e^{i\gamma\overline{C}_{ijk}}|s\rangle. \qquad (41)$$

For convenience, let $z_u = 1 - 2s_u$, and $\theta_{ijk}(z_i,z_j,z_k) = 2\gamma(z_iC_i + z_jC_j + z_kC_k + \frac{b_{ijk}}{2}z_iz_jz_k)$. Our present goal is to bound the expectation, $E_{ijk} = b_{ijk}\langle s|e^{-i\gamma\overline{C}_{ijk}}Y_iY_jY_ke^{i\gamma\overline{C}_{ijk}}|s\rangle$. From (40) and (41) we have,

$$\begin{aligned}
E_{ijk} &= b_{ijk}\langle s|e^{-i\gamma\overline{C}_{ijk}}Y_iY_jY_ke^{i\gamma\overline{C}_{ijk}}|s\rangle \\
&= \frac{1}{8}\sum_{z_i,z_j,z_k} -ib_{ijk}z_iz_jz_k\langle\bar{s}|e^{i\theta_{ijk}(z_i,z_j,z_k)}|\bar{s}\rangle \\
&= \frac{1}{8}\sum_{z_i,z_j,z_k} b_{ijk}z_iz_jz_k\langle\bar{s}|\sin\big(\theta_{ijk}(z_i,z_j,z_k)\big) - i\cos\big(\theta_{ijk}(z_i,z_j,z_k)\big)|\bar{s}\rangle. \qquad (42)
\end{aligned}$$

We will simplify (42) by grouping the term corresponding to z_i, z_j, and z_k with that corresponding to $-z_i$, $-z_j$, and $-z_k$. We will make use of the basic facts that sine is odd, cosine is even, and $\theta_{ijk}(-z_i,-z_j,-z_k) = -\theta_{ijk}(z_i,z_j,z_k)$.

$$\begin{aligned}
E_{ijk} &= \frac{1}{8}\sum_{\substack{z_i,z_j,z_k:\\ z_iz_jz_k=1}} b_{ijk}\langle\bar{s}|\sin\big(\theta_{ijk}(z_i,z_j,z_k)\big) - \sin\big(\theta_{ijk}(-z_i,-z_j,-z_k)\big)|\bar{s}\rangle \\
&= \frac{1}{4}\sum_{\substack{z_i,z_j,z_k:\\ z_iz_jz_k=1}} b_{ijk}\langle\bar{s}|\sin\big(\theta_{ijk}(z_i,z_j,z_k)\big)|\bar{s}\rangle \\
&= \langle\bar{s}|\frac{1}{4}\sum_{\substack{z_i,z_j,z_k:\\ z_iz_jz_k=1}} \sin\big(\gamma(1+2b_{ijk}(z_iC_i + z_jC_j + z_kC_k))\big)|\bar{s}\rangle. \qquad (43)
\end{aligned}$$

Let $\bar{z}$ be a vector over $\{-1,1\}$ corresponding to all variables except $\{i,j,k\}$, i.e. $\bar{z} \in \{-1,1\}^{\{1,\dots,n\}\setminus\{i,j,k\}}$. We evaluate the quantum expectation, (43) above by using the following analogue of C_u:

$$c_u(\bar{z}) = \sum_{\substack{v,w:\\ \{u,v,w\}\in\mathscr{C}}} b_{uvw}\bar{z}_v\bar{z}_w.$$

The quantum expectation, (43) becomes,

$$E_{ijk} = \frac{1}{2^{n-3}} \sum_{\bar{z}} \frac{1}{4} \Big[\sin\big(\gamma(1 + b_{ijk}(+c_i(\bar{z}) + c_j(\bar{z}) + c_k(\bar{z})))\big) + \\ \sin\big(\gamma(1 + b_{ijk}(+c_i(\bar{z}) - c_j(\bar{z}) - c_k(\bar{z})))\big) + \\ \sin\big(\gamma(1 + b_{ijk}(-c_i(\bar{z}) + c_j(\bar{z}) - c_k(\bar{z})))\big) + \\ \sin\big(\gamma(1 + b_{ijk}(-c_i(\bar{z}) - c_j(\bar{z}) + c_k(\bar{z})))\big) \Big].$$

Thus far we have essentially mimicked Farhi et al.'s analysis. Our approach diverges now, and we will bound E_{ijk} from below by directly considering a Maclaurin series expansion of $E_{ijk}(\gamma)$ to take advantage of cancellation among the terms. The function $E_{ijk}(\gamma)$ is a convex combination of functions of the form $\sin(\gamma c)$ with c independent of γ, hence the error bound below on the first-order approximation follows, where $E_{ijk}^{(l)}$ is the lth term of the Maclaurin series.

$$\left| E_{ijk} - E_{ijk}^{(1)} \right| \leq \left| E_{ijk}^{(3)} \right|, \tag{44}$$

We compute $E_{ijk}^{(1)}$ and $E_{ijk}^{(3)}$:

$$\begin{aligned} E_{ijk}^{(1)} &= \gamma \frac{1}{2^{n-3}} \sum_{\bar{z}} \frac{1}{4} \Big[(1 + b_{ijk}(+c_i(\bar{z}) + c_j(\bar{z}) + c_k(\bar{z}))) + \\ &\qquad (1 + b_{ijk}(+c_i(\bar{z}) - c_j(\bar{z}) - c_k(\bar{z}))) + \\ &\qquad (1 + b_{ijk}(-c_i(\bar{z}) + c_j(\bar{z}) - c_k(\bar{z}))) + \\ &\qquad (1 + b_{ijk}(-c_i(\bar{z}) - c_j(\bar{z}) + c_k(\bar{z}))) \Big] \\ &= \gamma, \text{ and} \qquad (45) \\ E_{ijk}^{(3)} &= -\frac{\gamma^3}{3!} \frac{1}{2^{n-3}} \sum_{\bar{z}} \frac{1}{4} \Big[(1 + b_{ijk}(+c_i(\bar{z}) + c_j(\bar{z}) + c_k(\bar{z})))^3 + \\ &\qquad (1 + b_{ijk}(+c_i(\bar{z}) - c_j(\bar{z}) - c_k(\bar{z})))^3 + \\ &\qquad (1 + b_{ijk}(-c_i(\bar{z}) + c_j(\bar{z}) - c_k(\bar{z})))^3 + \\ &\qquad (1 + b_{ijk}(-c_i(\bar{z}) - c_j(\bar{z}) + c_k(\bar{z})))^3 \Big] \\ &= -\gamma^3 \frac{1}{2^{n-3}} \sum_{\bar{z}} \left[b_{ijk}^3 c_i(\bar{z}) c_j(\bar{z}) c_k(\bar{z}) + \frac{b_{ijk}^2}{2} \left(c_i^2(\bar{z}) + c_j^2(\bar{z}) + c_k^2(\bar{z}) \right) + \frac{1}{6} \right]. \qquad (46) \end{aligned}$$

For convenience of notation, we follow [15] and think of the function $c_u(\bar{z})$ as a random variable, c_u over $\bar{z}$, in which case the sum in (46) becomes an expectation. We recall $b_{ijk} \in \{-1, 1\}$

and will choose $\gamma \geq 0$, hence we have the bound,

$$\left|E_{ijk}^{(3)}\right| \leq \gamma^3 \frac{1}{2^{n-3}} \left(\left| b_{ijk} \sum_{\bar{z}} c_i(\bar{z}) c_j(\bar{z}) c_k(\bar{z}) \right| + \sum_{\bar{z}} \left[\frac{1}{2} \left(c_i^2(\bar{z}) + c_j^2(\bar{z}) + c_k^2(\bar{z}) \right) + \frac{1}{6} \right] \right)$$
$$= \gamma^3 \left(\left| \mathbb{E}[c_i c_j c_k] \right| + \frac{1}{2} \mathbb{E}[c_i^2 + c_j^2 + c_k^2] + \frac{1}{6} \right). \tag{47}$$

Combining (47) with (44) and (45), we get:

$$E_{ijk} \geq E_{ijk}^{(1)} - \left| E_{ijk}^{(3)} \right| \geq \gamma - \gamma^3 \left(\left| \mathbb{E}[c_i c_j c_k] \right| + \frac{1}{2} \mathbb{E}[c_i^2 + c_j^2 + c_k^2] + \frac{1}{6} \right). \tag{48}$$

We provide bounds on $\mathbb{E}[c_u^2]$, for $u = i, j, k$, and $\left|\mathbb{E}[c_i c_j c_k]\right|$ in Lemmas 1 and 2, respectively. We may think of the constraints in $\mathscr{C}$ as defining a hypergraph, $\mathscr{H}$, on a set of vertices, $V = \{1, \ldots, n\}$, corresponding to the variables of our Max-E3-LIN2 instance. Each constraint $\{u, v, w\} \in \mathscr{C}$ corresponds to a hyperedge $e_{uvw} = \{u, v, w\}$, and we will henceforth use the terms constraint and hyperedge interchangeably. Note that the degree of any vertex in $\mathscr{H}$ is at most D.

Lemma 1 (Farhi et al.)**.** *For any vertex $u \in V$, $\mathbb{E}[c_u^2] \leq D$.*

Proof. By linearity of expectation we have,

$$\mathbb{E}[c_u^2] = \sum_{\substack{v,w \in V: \\ \{u,v,w\} \in \mathscr{C}}} \sum_{\substack{x,y \in V: \\ \{u,x,y\} \in \mathscr{C}}} b_{uvw} b_{uxy} \mathbb{E}[\bar{z}_v \bar{z}_w \bar{z}_x \bar{z}_y]$$

Since $v \neq w$ and $x \neq y$, the expectation in the summand is nonzero exactly when $\{v, w\} = \{x, y\}$. Thus,

$$\mathbb{E}[c_u^2] = \sum_{\substack{v,w \in V: \\ \{u,v,w\} \in \mathscr{C}}} b_{uvw}^2 \mathbb{E}[\bar{z}_v^2 \bar{z}_w^2] = \sum_{\substack{v,w \in V: \\ \{u,v,w\} \in \mathscr{C}}} 1$$
$$\leq D.$$

□

Now we need only bound $\left|\mathbb{E}[c_i c_j c_k]\right|$ in order to obtain our result. We require a few definitions in order to do so. We define a *triangle* in $\mathscr{H}$ to be a set of three hyperedges, e, f, and g such that $|e \cap f| = |e \cap g| = |f \cap g| = 1$, and $(e \cap f) \neq (e \cap g) \neq (f \cap g) \neq (e \cap f)$. An example appears in Figure 31. Any hyperedge in a triangle contains exactly one vertex not in the other two hyperedges, and these vertices are distinct for each hyperedge in the triangle. If there happens to be a hyperedge on these vertices, it is called the *foundation* of the triangle. More precisely, for a triangle on hyperedges e, f, and g, if $(e \setminus (f \cup g)) \cup (f \setminus (e \cup g)) \cup (g \setminus (e \cup f))$ is also hyperedge, then it is the foundation of the triangle. Observe that each triangle has at most one foundation. Let T_{uvw} be the number of triangles in $\mathscr{H}$ with foundation $\{u, v, w\} \in \mathscr{C}$.

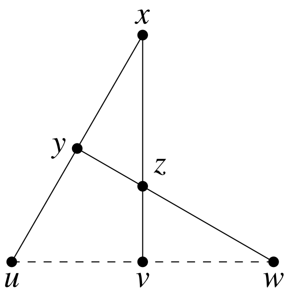

Figure 31. An example of a *triangle* in a hypergraph, where maximal lines represent hyperedges. The triangle is defined by the three hyperedges, $\{x,y,u\}$, $\{x,z,v\}$, and $\{y,z,w\}$. The dashed hyperedge, $\{u,v,w\}$, is the *foundation* of the triangle.

Lemma 2. *For any constraint* $\{u,v,w\} \in \mathscr{C}$, $|\mathbb{E}[c_u c_v c_w]| \leq T_{uvw}$.

Proof. By linearity of expectation we have,

$$\mathbb{E}[c_u c_v c_w] = \sum_{\substack{u',u'' \in V: \\ \{u,u',u''\} \in \mathscr{C}}} \sum_{\substack{v',v'' \in V: \\ \{v,v',v''\} \in \mathscr{C}}} \sum_{\substack{w',w'' \in V: \\ \{w,w',w''\} \in \mathscr{C}}} b_{uu'u''} b_{vv'v''} b_{ww'w''} \mathbb{E}[\bar{z}_{u'} \bar{z}_{u''} \bar{z}_{v'} \bar{z}_{v''} \bar{z}_{w'} \bar{z}_{w''}].$$

Consider the expectation in the summand above; since $u' \neq u''$, $v' \neq v''$, and $w' \neq w''$, it follows that $\mathbb{E}[\bar{z}_{u'} \bar{z}_{u''} \bar{z}_{v'} \bar{z}_{v''} \bar{z}_{w'} \bar{z}_{w''}] \neq 0$ exactly when $|\{u',u''\} \cap \{v',v''\}| = |\{u',u''\} \cap \{w',w''\}| = |\{v',v''\} \cap \{w',w''\}| = 1$. Thus,

$$|\mathbb{E}[c_u c_v c_w]| \leq \sum_{\substack{x,y,z \in V: \\ \{u,x,y\} \in \mathscr{C}, \\ \{v,x,z\} \in \mathscr{C}, \\ \{w,y,z\} \in \mathscr{C}}} \left| b_{uxy} b_{vxz} b_{wyz} \mathbb{E}[\bar{z}_x^2 \bar{z}_y^2 \bar{z}_z^2] \right| = \sum_{\substack{x,y,z \in V: \\ \{u,x,y\} \in \mathscr{C}, \\ \{v,x,z\} \in \mathscr{C}, \\ \{w,y,z\} \in \mathscr{C}}} 1,$$

where the last sum precisely counts the number of triangles with foundation $\{u,v,w\}$. $\square$

By plugging in the bounds from lemmas 1 and 2 into (48) and solving for a value of γ which maximizes the latter bound on E_{ijk}, one may obtain QAOA performance bounds for Max-E3-LIN2 comparable to those from Farhi et al's original work on the subject. As with the latter, we obtain improved bounds when the instance contains no triangles, i.e. when $T_{uvw} = 0$ for all u,v,w.

4 Conclusion

In this project we have established the infrastructure to realize single and multi-qubit operations using trapped $^{171}\mathrm{Yb}^{+}$ ions. Using scalable microfabricated surface electrode ion traps, we have realized single qubit gates using resonant microwave radiation and demonstrated a diamond norm distance of $< 1.9 \times 10^{-4}$ surpassing the fault tolerance threshold for some quantum codes. We have demonstrated Raman laser induced single qubit gates with an infidelity $< 1.3 \times 10^{-4}$. Finally, we have realized a two-qubit gate with a fidelity of more than 97.7%.

These results clearly demonstrate that high fidelity quantum information processing in scalable Sandia surface ion traps is possible.

References

[1] Panos Aliferis and Andrew W. Cross. Subsystem fault tolerance with the Bacon-Shor code. *Physical Review Letters*, 98(22), May 2007. arXiv: quant-ph/0610063.

[2] D. T. C. Allcock, L. Guidoni, T. P. Harty, C. J. Ballance, M. G. Blain, A. M. Steane, and D. M. Lucas. Reduction of heating rate in a microfabricated ion trap by pulsed-laser cleaning. *New Journal of Physics*, 13(12):123023, December 2011.

[3] David D. Awschalom, Lee C. Bassett, Andrew S. Dzurak, Evelyn L. Hu, and Jason R. Petta. Quantum Spintronics: Engineering and Manipulating Atom-Like Spins in Semiconductors. *Science*, 339(6124):1174–1179, March 2013.

[4] C. J. Ballance, T. P. Harty, N. M. Linke, M. A. Sepiol, and D. M. Lucas. Laser-driven quantum logic gates with precision beyond the fault-tolerant threshold. *arXiv:1512.04600 [quant-ph]*, December 2015. arXiv: 1512.04600.

[5] Boaz Barak, Ankur Moitra, Ryan O'Donnell, Prasad Raghavendra, Oded Regev, David Steurer, Luca Trevisan, Aravindan Vijayaraghavan, David Witmer, and John Wright. Beating the random assignment on constraint satisfaction problems of bounded degree. *arXiv:1505.03424 [cs]*, May 2015. arXiv: 1505.03424.

[6] M. D. Barrett, J. Chiaverini, T. Schaetz, J. Britton, W. M. Itano, J. D. Jost, E. Knill, C. Langer, D. Leibfried, R. Ozeri, and D. J. Wineland. Deterministic quantum teleportation of atomic qubits. *Nature*, 429(6993):737–739, June 2004.

[7] Robin Blume-Kohout, John King Gamble, Eric Nielsen, Kenneth Rudinger, Jonathan Mizrahi, Kevin Fortier, and Peter Maunz. A certifiably fault tolerant qubit. *to be published*, 2016.

[8] Robin Blume-Kohout, John King Gamble, Erik Nielsen, Jonathan Mizrahi, Jonathan D. Sterk, and Peter Maunz. Robust, self-consistent, closed-form tomography of quantum logic gates on a trapped ion qubit. *arXiv:1310.4492 [quant-ph]*, October 2013.

[9] K.-A. Brickman, P. C. Haljan, P. J. Lee, M. Acton, L. Deslauriers, and C. Monroe. Implementation of Grover's quantum search algorithm in a scalable system. *Physical Review A*, 72(5):050306, November 2005.

[10] M. Brownnutt, M. Kumph, P. Rabl, and R. Blatt. Ion-trap measurements of electric-field noise near surfaces. *arXiv:1409.6572 [quant-ph]*, September 2014. arXiv: 1409.6572.

[11] J. I. Cirac and P. Zoller. Quantum Computations with Cold Trapped Ions. *Physical Review Letters*, 74(20):4091–4094, May 1995.

[12] M. H. Devoret and R. J. Schoelkopf. Superconducting Circuits for Quantum Information: An Outlook. *Science*, 339(6124):1169–1174, March 2013.

[13] Sebastian Dörn and Thomas Thierauf. The Quantum Complexity of Group Testing. In Viliam Geffert, Juhani Karhumäki, Alberto Bertoni, Bart Preneel, Pavol Návrat, and Mária Bieliková, editors, *SOFSEM 2008: Theory and Practice of Computer Science*, number 4910 in Lecture Notes in Computer Science, pages 506–518. Springer Berlin Heidelberg, January 2008. DOI: 10.1007/978-3-540-77566-9_44.

[14] Jürgen Eschner, Giovanna Morigi, Ferdinand Schmidt-Kaler, and Rainer Blatt. Laser cooling of trapped ions. *Journal of the Optical Society of America B*, 20(5):1003, 2003.

[15] Edward Farhi, Jeffrey Goldstone, and Sam Gutmann. A Quantum Approximate Optimization Algorithm. *arXiv:1411.4028 [quant-ph]*, November 2014. arXiv: 1411.4028.

[16] Edward Farhi, Jeffrey Goldstone, and Sam Gutmann. A Quantum Approximate Optimization Algorithm Applied to a Bounded Occurrence Constraint Problem. *arXiv:1412.6062 [quant-ph]*, December 2014. arXiv: 1412.6062.

[17] J. J. García-Ripoll, P. Zoller, and J. I. Cirac. Speed Optimized Two-Qubit Gates with Laser Coherent Control Techniques for Ion Trap Quantum Computing. *Physical Review Letters*, 91(15):157901, October 2003.

[18] Silvano Garnerone, Paolo Zanardi, and Daniel A. Lidar. Adiabatic Quantum Algorithm for Search Engine Ranking. *Physical Review Letters*, 108(23):230506, June 2012.

[19] D. Hayes, S. M. Clark, S. Debnath, D. Hucul, I. V. Inlek, K. W. Lee, Q. Quraishi, and C. Monroe. Coherent Error Suppression in Multiqubit Entangling Gates. *Physical Review Letters*, 109(2):020503, July 2012.

[20] D. Hayes, D. N. Matsukevich, P. Maunz, D. Hucul, Q. Quraishi, S. Olmschenk, W. Campbell, J. Mizrahi, C. Senko, and C. Monroe. Entanglement of Atomic Qubits Using an Optical Frequency Comb. *Physical Review Letters*, 104(14):140501, April 2010.

[21] David Lee Hayes. *Remote and Local Entanglement of Ions with Photons and Phonons,*. PhD Thesis, University of Maryland, College Park, MD, 2012.

[22] Creston D. Herold, Spencer D. Fallek, J. True Merrill, Adam M. Meier, Kenton R. Brown, Curtis Volin, and Jason M. Amini. Universal Control of Ion Qubits in a Scalable Microfabricated Planar Trap. *arXiv:1509.05378 [physics, physics:quant-ph]*, September 2015. arXiv: 1509.05378.

[23] D. A. Hite, Y. Colombe, A. C. Wilson, K. R. Brown, U. Warring, R. Jördens, J. D. Jost, K. S. McKay, D. P. Pappas, D. Leibfried, and D. J. Wineland. 100-Fold Reduction of Electric-Field Noise in an Ion Trap Cleaned with In Situ Argon-Ion-Beam Bombardment. *Physical Review Letters*, 109(10):103001, September 2012.

[24] I. V. Inlek, G. Vittorini, D. Hucul, C. Crocker, and C. Monroe. Quantum gates with phase stability over space and time. *Physical Review A*, 90(4):042316, October 2014.

[25] Kaveh Khodjasteh and Lorenza Viola. Dynamical quantum error correction of unitary operations with bounded controls. *Physical Review A*, 80(3):032314, 2009.

[26] D. Kielpinski, C. Monroe, and D. J. Wineland. Architecture for a large-scale ion-trap quantum computer. *Nature*, 417(6890):709–711, June 2002.

[27] Jaroslaw Labaziewicz, Yufei Ge, Paul Antohi, David Leibrandt, Kenneth R. Brown, and Isaac L. Chuang. Suppression of Heating Rates in Cryogenic Surface-Electrode Ion Traps. *Physical Review Letters*, 100(1):013001, January 2008.

[28] T. Loke, J. W. Tang, J. Rodriguez, M. Small, and J. B. Wang. Comparing classical and quantum PageRanks. *arXiv:1511.04823 [physics, physics:quant-ph]*, November 2015. arXiv: 1511.04823.

[29] P. Maunz, S. Olmschenk, D. Hayes, D. N Matsukevich, L. M Duan, and C. Monroe. A heralded quantum gate between remote quantum memories. *arXiv:0902.2136 (quant-ph)*, February 2009.

[30] J. True Merrill and Kenneth R. Brown. Progress in compensating pulse sequences for quantum computation. *arXiv:1203.6392 [quant-ph]*, March 2012. arXiv: 1203.6392.

[31] Jonathan Albert Mizrahi. *Ultrafast Control of Spin and Motion in Trapped Ions*. PhD Thesis, University of Maryland, College Park, MD, 2013.

[32] D L Moehring, C Highstrete, D Stick, K M Fortier, R Haltli, C Tigges, and M G Blain. Design, fabrication and experimental demonstration of junction surface ion traps. *New Journal of Physics*, 13(7):075018, July 2011.

[33] C. Monroe and J. Kim. Scaling the Ion Trap Quantum Processor. *Science*, 339(6124):1164–1169, March 2013.

[34] T. Monz, K. Kim, W. Hänsel, M. Riebe, A. S. Villar, P. Schindler, M. Chwalla, M. Hennrich, and R. Blatt. Realization of the Quantum Toffoli Gate with Trapped Ions. *Physical Review Letters*, 102(4):040501, January 2009.

[35] Thomas Monz, Daniel Nigg, Esteban A. Martinez, Matthias F. Brandl, Philipp Schindler, Richard Rines, Shannon X. Wang, Isaac L. Chuang, and Rainer Blatt. Realization of a scalable Shor algorithm. *arXiv:1507.08852 [quant-ph]*, July 2015. arXiv: 1507.08852.

[36] Emily Mount, So-Young Baek, Matthew Blain, Daniel Stick, Daniel Gaultney, Stephen Crain, Rachel Noek, Taehyun Kim, Peter Maunz, and Jungsang Kim. Single qubit manipulation in a microfabricated surface electrode ion trap. *New Journal of Physics*, 15(9):093018, September 2013.

[37] Emily Mount, Chingiz Kabytayev, Stephen Crain, Robin Harper, So-Young Baek, Geert Vrijsen, Steven T. Flammia, Kenneth R. Brown, Peter Maunz, and Jungsang Kim. Error compensation of single-qubit gates in a surface-electrode ion trap using composite pulses. *Physical Review A*, 92(6):060301, December 2015.

[38] Rachel Noek, Geert Vrijsen, Daniel Gaultney, Emily Mount, Taehyun Kim, Peter Maunz, and Jungsang Kim. High speed, high fidelity detection of an atomic hyperfine qubit. *Optics Letters*, 38(22):4735–4738, November 2013.

[39] S. Olmschenk, D. N. Matsukevich, P. Maunz, D. Hayes, L.-M. Duan, and C. Monroe. Quantum Teleportation Between Distant Matter Qubits. *Science*, 323(5913):486–489, January 2009.

[40] S. Olmschenk, K. C. Younge, D. L. Moehring, D. N. Matsukevich, P. Maunz, and C. Monroe. Manipulation and detection of a trapped Yb[sup +] hyperfine qubit. *Physical Review A (Atomic, Molecular, and Optical Physics)*, 76(5):052314–9, November 2007.

[41] C. Ospelkaus, U. Warring, Y. Colombe, K. R. Brown, J. M. Amini, D. Leibfried, and D. J. Wineland. Microwave quantum logic gates for trapped ions. *Nature*, 476(7359):181–184, August 2011.

[42] M. Riebe, M. Chwalla, J. Benhelm, H. Häffner, W. Hänsel, C. F. Roos, and R. Blatt. Quantum teleportation with atoms: quantum process tomography. *New Journal of Physics*, 9:211, 2007.

[43] Philipp Schindler, Julio T. Barreiro, Thomas Monz, Volckmar Nebendahl, Daniel Nigg, Michael Chwalla, Markus Hennrich, and Rainer Blatt. Experimental Repetitive Quantum Error Correction. *Science*, 332(6033):1059–1061, May 2011.

[44] Philipp Schindler, Dylan J. Gorman, Nikos Daniilidis, and Hartmut Häffner. Polarization of electric field noise near metallic surfaces. *arXiv:1505.01237 [physics, physics:quant-ph]*, May 2015. arXiv: 1505.01237.

[45] S. Seidelin, J. Chiaverini, R. Reichle, J. J. Bollinger, D. Leibfried, J. Britton, J. H. Wesenberg, R. B. Blakestad, R. J. Epstein, D. B. Hume, W. M. Itano, J. D. Jost, C. Langer, R. Ozeri, N. Shiga, and D. J. Wineland. Microfabricated Surface-Electrode Ion Trap for Scalable Quantum Information Processing. *Physical Review Letters*, 96(25):253003, June 2006.

[46] P. W. Shor. Algorithms for Quantum Computation: Discrete Logarithms and Factoring. In *Annual Symposium on Foundations of Computer Science*, volume 35, pages 124–134. IEEE Computer Society Press, 1994.

[47] G. Shu, G. Vittorini, A. Buikema, C. S. Nichols, C. Volin, D. Stick, and Kenneth R. Brown. Heating rates and ion-motion control in a Y-junction surface-electrode trap. *Physical Review A*, 89(6):062308, June 2014.

[48] Anders Sørensen and Klaus Mølmer. Quantum Computation with Ions in Thermal Motion. *Physical Review Letters*, 82(9):1971–1974, March 1999.

[49] Anders Sørensen and Klaus Mølmer. Entanglement and quantum computation with ions in thermal motion. *Physical Review A*, 62(2):022311, July 2000.

[50] D. Stick, K M Fortier, R. Haltli, C. Highstrete, D L Moehring, C. Tigges, and M G Blain. Demonstration of a microfabricated surface electrode ion trap. *arXiv:1008.0990*, August 2010.

[51] Q. A. Turchette, C. S. Wood, B. E. King, C. J. Myatt, D. Leibfried, W. M. Itano, C. Monroe, and D. J. Wineland. Deterministic Entanglement of Two Trapped Ions. *Physical Review Letters*, 81(17):3631, October 1998. Copyright (C) 2009 The American Physical Society; Please report any problems to prola@aps.org.

[52] Salvador Elías Venegas-Andraca. Quantum Walks: A Comprehensive Review. *Quantum Information Processing*, 11(5):1015–1106, October 2012.

[53] S. Wimperis. Broadband, Narrowband, and Passband Composite Pulses for Use in Advanced NMR Experiments. *Journal of Magnetic Resonance, Series A*, 109(2):221–231, August 1994.

A GST data of the microwave single qubit gates

Results tables as obtained from the GST procedure are reprinted in this appendix.

A.1 GST results for the “wait” experiment

Gate	Process Infidelity	½ Trace Distance	½ ◇-Norm	Frobenius Distance
Gi	−0.000017 ±0.000531	0.000488 ±0.000532	0 $\pm --$	0.00128 ±0.000155
Gx	0.000318 ±0.000115	0.003083 ±0.000126	0 $\pm --$	0.007839 ±0.002819
Gy	0.000494 ±0.000009	0.003856 ±0.000105	0 $\pm --$	0.009408 ±0.012193

Gate	Error Generator
Gi	$\begin{pmatrix} 0 & 0 & 0 & 0 \\ -4\times 10^{-6} & -2\times 10^{-7} & -0.0002 & 0.0007 \\ 8\times 10^{-6} & 0.0003 & -8\times 10^{-6} & -0.0005 \\ 4\times 10^{-6} & -0.0007 & 0.0006 & 0.0001 \end{pmatrix}$
Gx	$\begin{pmatrix} 0 & 0 & 0 & 0 \\ -3\times 10^{-6} & -4\times 10^{-6} & 0.0002 & -0.0005 \\ -0.0007 & -0.0002 & -0.0006 & 0.0037 \\ -0.003 & 0.0013 & -0.0059 & -0.0006 \end{pmatrix}$
Gy	$\begin{pmatrix} 0 & 0 & 0 & 0 \\ -0.0002 & -0.001 & 0.0003 & -0.0049 \\ 7\times 10^{-6} & -0.0012 & -8\times 10^{-6} & -0.0001 \\ -0.0021 & 0.0075 & -2\times 10^{-5} & -0.001 \end{pmatrix}$

Table A.1. Comparison of GST estimated gates to target gates . This table presents, for each of the gates, three different measures of distance or discrepancy from the GST estimate to the ideal target operation. See text for more detail. The second table lists the “Error Generator” for each gate, which is the Lindbladian $\mathbb{L}$ that describes *how* the gate is failing to match the target. This error generator is defined by the equation $\hat{G} = G_{\text{target}} e^{\mathbb{L}}$.

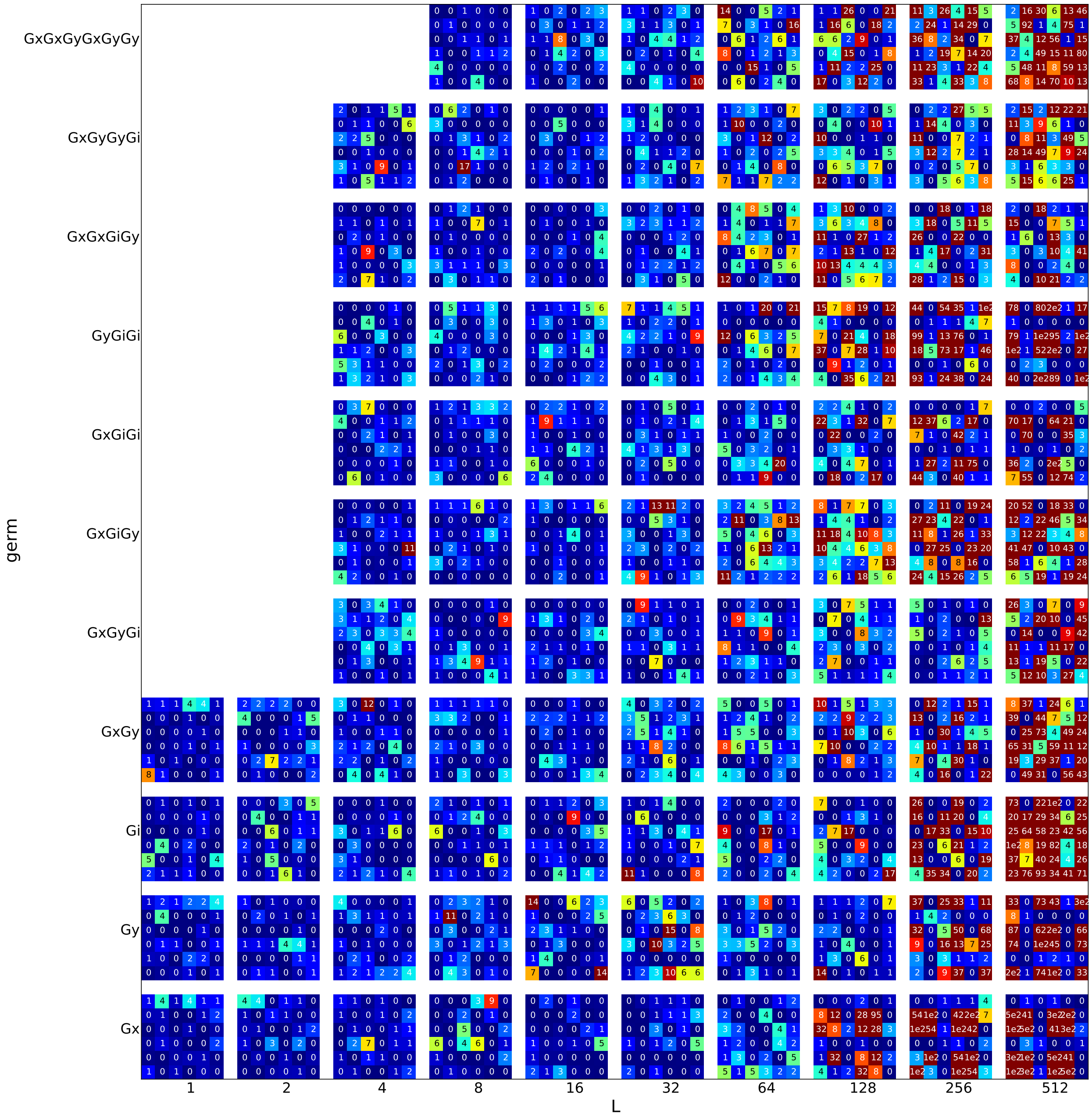

Figure A.1. $2\Delta\log(\mathscr{L})$ **contributions for every individual experiment in the dataset**. Each pixel represents a single experiment (gate sequence), and its color indicates whether GST was able to fit the corresponding frequency well. Blue is typical; dark red squares indicating $2\Delta\log(\mathscr{L})_s > 10$ should appear only once per 638 experiments on average. Square blocks of pixels correspond to base sequences (arranged vertically by germ and horizontally by length); each pixel within a block corresponds to a specific choice of pre- and post-fiducial sequences. See text for further details.

Gate	Eigenvalues	Fixed pt	Rotn. axis	Diag. decay	Off-diag. decay
Gi	$1e^{i0.0}$ ± $0.0005e^{i0.1}$	0.9999	0		
	$1e^{-i0.0}$ ± $0.0005e^{i0.1}$	0.001	0.6132	-0.000073	0.000003
	1.0001 ± 0.0001	-0.0041	0.7479	± 0.000175	± 0.000894
	1 ± 0	0.0097	0.2542		
Gx	$0.9994e^{i1.6}$ ± $0.0013e^{i0.0}$	1	0		
	$0.9994e^{-i1.6}$ ± $0.0013e^{i0.0}$	2×10^{-6}	-1	0.000004	0.000622
	1 ± 1×10^{-5}	0.0018	0.0006	± 0.00001	± 0.000036
	1 ± 0	0.0012	0.0008		
Gy	$0.999e^{i1.6}$ ± $0.0056e^{i0.0}$	1	0		
	$0.999e^{-i1.6}$ ± $0.0056e^{i0.0}$	-0.001	-0.0002	0.000008	0.000966
	1 ± 9×10^{-6}	1×10^{-9}	1	± 0.000009	± 0.000072
	1 ± 0	0.0012	-0.0001		

Gate	Angle	Angle between Rotation Axes		
		Gi	Gx	Gy
Gi	$(0.000286 \pm 0.000022)\pi$		0.500000π	0.231123π
Gx	$(0.49846 \pm 0.000654)\pi$	0.500000π		0.499771π
Gy	$(0.498025 \pm 0.002813)\pi$	0.231123π	0.499771π	

Table A.2. Eigen-decomposition of estimated gates. Each estimated gate is described in terms of: (1) the eigenvalues of the superoperator; (2) the gate's fixed point (as a vector in $\mathscr{B}(\mathscr{H})$, in the Pauli basis); (3) the axis around which it rotates, as a vector in $\mathscr{B}(\mathscr{H})$; (4) the angle of the rotation that it applies; (5) the decay rate along the axis of rotation ("diagonal decay"); (6) the decay rate perpendicular to the axis of rotation ("off-diagonal decay"); and (7) the angle between each gate's rotation axis and the rotation axes of the other gates. "X" indicates that the decomposition failed or couldn't be interpreted.

A.2 GST results for the “BB1 wait” experiment

Gate	Process Infidelity	$1/2$ Trace Distance	$1/2$ $\Diamond$-Norm	Frobenius Distance
Gi	0.0014 ±0.001248	0.004586 ±0.000913	0 $\pm --$	0.012858 ±0.001126
Gx	0.000192 ±0.000185	0.003495 ±0.004079	0 $\pm --$	0.008094 ±0.008167
Gy	0.000058 ±0.000492	0.002491 ±0.000312	0 $\pm --$	0.005544 ±0.00138

Gate	Error Generator
Gi	$\begin{pmatrix} 0 & 0 & 0 & 0 \\ 4\times10^{-6} & -2\times10^{-5} & 0.0007 & 0.0001 \\ 0.0001 & -5\times10^{-5} & -0.0028 & 0.0087 \\ 4\times10^{-5} & -2\times10^{-5} & -0.0087 & -0.0027 \end{pmatrix}$
Gx	$\begin{pmatrix} 0 & 0 & 0 & 0 \\ 6\times10^{-6} & -0.0001 & 0.0001 & -0.0006 \\ -0.0026 & 0.0006 & -0.0005 & -0.0034 \\ -0.0056 & 0.0002 & -0.0039 & -0.0002 \end{pmatrix}$
Gy	$\begin{pmatrix} 0 & 0 & 0 & 0 \\ -0.0011 & -0.0001 & -0.0032 & 0.0008 \\ 4\times10^{-6} & -0.0007 & -3\times10^{-5} & 0.0001 \\ -0.0019 & 0.0007 & -0.0037 & -0.0001 \end{pmatrix}$

Table A.3. Comparison of GST estimated gates to target gates. This table presents, for each of the gates, three different measures of distance or discrepancy from the GST estimate to the ideal target operation. See text for more detail. The second table lists the “Error Generator” for each gate, which is the Lindbladian $\mathbb{L}$ that describes *how* the gate is failing to match the target. This error generator is defined by the equation $\hat{G} = G_{\text{target}} e^{\mathbb{L}}$.

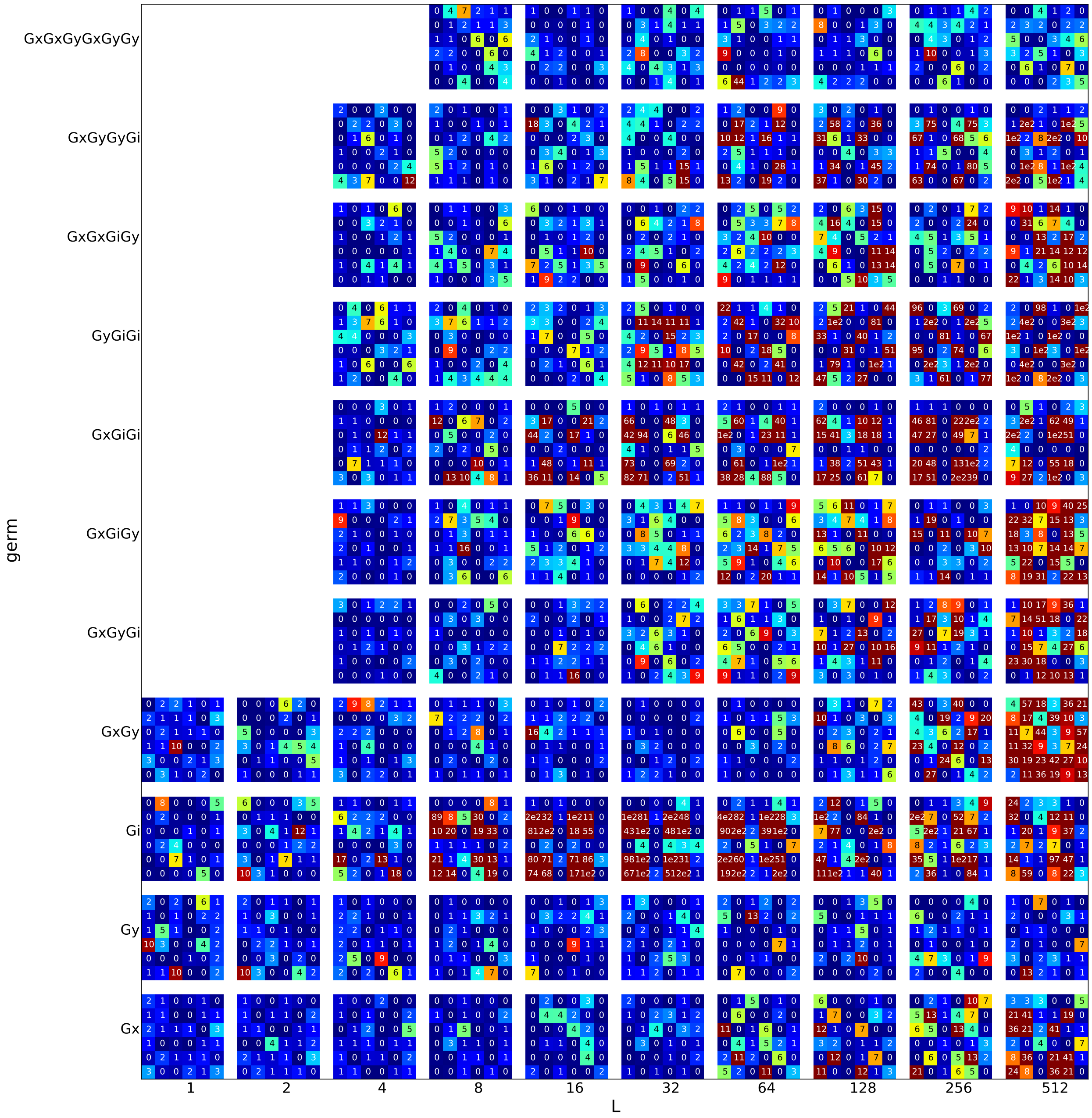

Figure A.2. $2\Delta\log(\mathscr{L})$ **contributions for every individual experiment in the dataset**. Each pixel represents a single experiment (gate sequence), and its color indicates whether GST was able to fit the corresponding frequency well. Blue is typical; dark red squares indicating $2\Delta\log(\mathscr{L})_s > 10$ should appear only once per 638 experiments on average. Square blocks of pixels correspond to base sequences (arranged vertically by germ and horizontally by length); each pixel within a block corresponds to a specific choice of pre- and post-fiducial sequences. See text for further details.

Gate	Eigenvalues			Fixed pt	Rotn. axis	Diag. decay	Off-diag. decay
Gi	$0.9972e^{i0.0}$	$\pm$	$0.0013e^{i0.1}$	0.9998	0	0.000018 ±0.000012	0.002754 ±0.002319
	$0.9972e^{-i0.0}$		$0.0013e^{i0.1}$	0.0001	-1		
	1		1×10^{-5}	0.0077	0.0037		
	1		0	-0.0107	-0.0044		
Gx	$0.9997e^{i1.6}$	$\pm$	$0.0047e^{i0.0}$	0.996	0	0.00012 ±0.000027	0.000331 ±0.000046
	$0.9997e^{-i1.6}$		$0.0047e^{i0.0}$	0.0629	-1		
	0.9999		3×10^{-5}	0.0041	0.0004		
	1		0	0.0015	-0.0002		
Gy	$0.9999e^{i1.6}$	$\pm$	$0.0023e^{i0.0}$	1	0	0.000032 ±0.000015	0.000101 ±0.000017
	$0.9999e^{-i1.6}$		$0.0023e^{i0.0}$	-0.0004	-0.0002		
	1		2×10^{-5}	-5×10^{-6}	1		
	1		0	0.0015	0.0035		

Gate	Angle	Angle between Rotation Axes		
		Gi	Gx	Gy
Gi	$(0.002757 \pm 0.00005)\pi$		0.001708π	0.498744π
Gx	$(0.499917 \pm 0.002354)\pi$	0.001708π		0.499787π
Gy	$(0.500026 \pm 0.00116)\pi$	0.498744π	0.499787π	

Table A.4. Eigen-decomposition of estimated gates. Each estimated gate is described in terms of: (1) the eigenvalues of the superoperator; (2) the gate's fixed point (as a vector in $\mathscr{B}(\mathscr{H})$, in the Pauli basis); (3) the axis around which it rotates, as a vector in $\mathscr{B}(\mathscr{H})$; (4) the angle of the rotation that it applies; (5) the decay rate along the axis of rotation ("diagonal decay"); (6) the decay rate perpendicular to the axis of rotation ("off-diagonal decay"); and (7) the angle between each gate's rotation axis and the rotation axes of the other gates. "X" indicates that the decomposition failed or couldn't be interpreted.

A.3 GST results for the “BB1 XX” experiment

Gate	Process Infidelity	$1/2$ Trace Distance	$1/2$ $\Diamond$-Norm	Frobenius Distance
Gi	0.001203 ± 0.001368	0.007437 ± 0.001813	0 $\pm --$	0.020368 ± 0.000842
Gx	0.000103 ± 0.000164	0.0036 ± 0.002227	0 $\pm --$	0.00825 ± 0.004792
Gy	0.000035 ± 0.000174	0.002372 ± 0.000785	0 $\pm --$	0.005334 ± 0.002906

Gate	Error Generator
Gi	$\begin{pmatrix} 0 & 0 & 0 & 0 \\ -6\times10^{-6} & -3\times10^{-5} & 0.0011 & -0.0001 \\ 2\times10^{-5} & -0.0005 & -0.0018 & 0.0142 \\ 0.0001 & 0.0003 & -0.0142 & -0.0028 \end{pmatrix}$
Gx	$\begin{pmatrix} 0 & 0 & 0 & 0 \\ -1\times10^{-5} & -0.0001 & -0.0006 & -0.0005 \\ -0.0029 & 0.0009 & -0.0003 & -0.0032 \\ -0.0057 & 0.0002 & -0.004 & -4\times10^{-5} \end{pmatrix}$
Gy	$\begin{pmatrix} 0 & 0 & 0 & 0 \\ -0.0006 & -5\times10^{-5} & -0.0027 & 0.0007 \\ -4\times10^{-6} & -0.0011 & -2\times10^{-5} & 3\times10^{-5} \\ -0.0021 & 0.0006 & -0.0038 & -0.0001 \end{pmatrix}$

Table A.5. Comparison of GST estimated gates to target gates. This table presents, for each of the gates, three different measures of distance or discrepancy from the GST estimate to the ideal target operation. See text for more detail. The second table lists the “Error Generator” for each gate, which is the Lindbladian $\mathbb{L}$ that describes *how* the gate is failing to match the target. This error generator is defined by the equation $\hat{G} = G_{\text{target}} e^{\mathbb{L}}$.

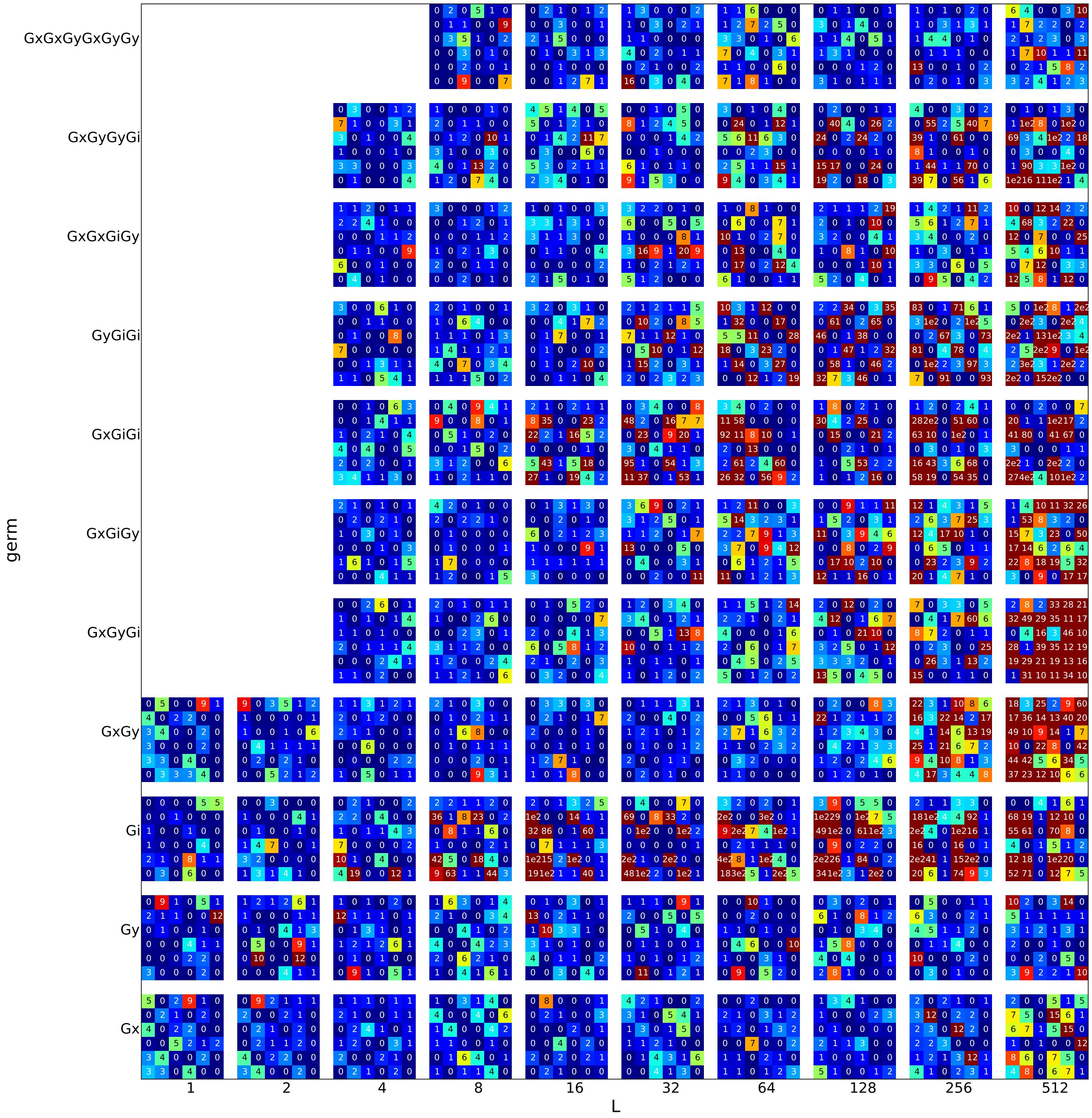

Figure A.3. $2\Delta\log(\mathscr{L})$ **contributions for every individual experiment in the dataset**. Each pixel represents a single experiment (gate sequence), and its color indicates whether GST was able to fit the corresponding frequency well. Blue is typical; dark red squares indicating $2\Delta\log(\mathscr{L})_s > 10$ should appear only once per 638 experiments on average. Square blocks of pixels correspond to base sequences (arranged vertically by germ and horizontally by length); each pixel within a block corresponds to a specific choice of pre- and post-fiducial sequences. See text for further details.

Gate	Eigenvalues			Fixed pt	Rotn. axis	Diag. decay	Off-diag. decay
Gi	$0.9977e^{i0.0}$	±	$0.0014e^{i0.1}$	1	0	0.000012 ±0.000019	0.0023 ±0.002534
	$0.9977e^{-i0.0}$		$0.0014e^{i0.1}$	-0.0001	0.9991		
	1		1×10^{-5}	0.007	0.0168		
	1		0	-0.0003	0.0385		
Gx	$0.9998e^{i1.6}$	±	$0.0029e^{i0.0}$	0.9827	0	0.000104 ±0.000025	0.000159 ±0.000033
	$0.9998e^{-i1.6}$		$0.0029e^{i0.0}$	-0.1303	-1		
	0.9999		2×10^{-5}	0.0043	0.0006		
	1		0	0.0013	-0.0003		
Gy	$0.9999e^{i1.6}$	±	$0.0041e^{i0.0}$	1	0	0.000022 ±0.000013	0.000061 ±0.000012
	$0.9999e^{-i1.6}$		$0.0041e^{i0.0}$	-0.0007	-0.0005		
	1		1×10^{-5}	-5×10^{-6}	1		
	1		0	0.0014	0.0032		

Gate	Angle	Angle between Rotation Axes		
		Gi	Gx	Gy
Gi	$(0.004524 \pm 0.000046)\pi$		0.500000π	0.494765π
Gx	$(0.49987 \pm 0.001468)\pi$	0.500000π		0.499652π
Gy	$(0.500017 \pm 0.00204)\pi$	0.494765π	0.499652π	

Table A.6. Eigen-decomposition of estimated gates. Each estimated gate is described in terms of: (1) the eigenvalues of the superoperator; (2) the gate's fixed point (as a vector in $\mathscr{B}(\mathscr{H})$, in the Pauli basis); (3) the axis around which it rotates, as a vector in $\mathscr{B}(\mathscr{H})$; (4) the angle of the rotation that it applies; (5) the decay rate along the axis of rotation ("diagonal decay"); (6) the decay rate perpendicular to the axis of rotation ("off-diagonal decay"); and (7) the angle between each gate's rotation axis and the rotation axes of the other gates. "X" indicates that the decomposition failed or couldn't be interpreted.

A.4 GST results for the “BB1 XYXY” experiment

Gate	Process Infidelity	½ Trace Distance	½ ◊-Norm	Frobenius Distance
Gi	0.000061 ±0.000159	0.000072 ±0.000171	0 $\pm - -$	0.00017 ±0.000331
Gx	0.00006 ±0.000081	0.001339 ±0.001493	0 $\pm - -$	0.002701 ±0.002692
Gy	0.000065 ±0.000369	0.001249 ±0.000912	0 $\pm - -$	0.002531 ±0.001803

Gate	Error Generator
Gi	$\begin{pmatrix} 0 & 0 & 0 & 0 \\ 2\times10^{-6} & -0.0001 & -0.0001 & 2\times10^{-5} \\ 3\times10^{-6} & 4\times10^{-5} & -0.0001 & 2\times10^{-5} \\ -1\times10^{-6} & -2\times10^{-5} & -4\times10^{-5} & -0.0001 \end{pmatrix}$
Gx	$\begin{pmatrix} 0 & 0 & 0 & 0 \\ -9\times10^{-7} & -0.0001 & -0.0001 & 0.0001 \\ 0.0007 & 2\times10^{-5} & -0.0001 & -0.0002 \\ -0.0025 & -1\times10^{-6} & -0.0004 & -0.0001 \end{pmatrix}$
Gy	$\begin{pmatrix} 0 & 0 & 0 & 0 \\ -0.0015 & -0.0001 & 0.0003 & 0.0001 \\ 3\times10^{-7} & -0.0006 & -4\times10^{-5} & -0.0006 \\ -0.0018 & 0.0001 & 0.0003 & -0.0001 \end{pmatrix}$

Table A.7. Comparison of GST estimated gates to target gates. This table presents, for each of the gates, three different measures of distance or discrepancy from the GST estimate to the ideal target operation. See text for more detail. The second table lists the “Error Generator” for each gate, which is the Lindbladian $\mathbb{L}$ that describes *how* the gate is failing to match the target. This error generator is defined by the equation $\hat{G} = G_{\text{target}} e^{\mathbb{L}}$.

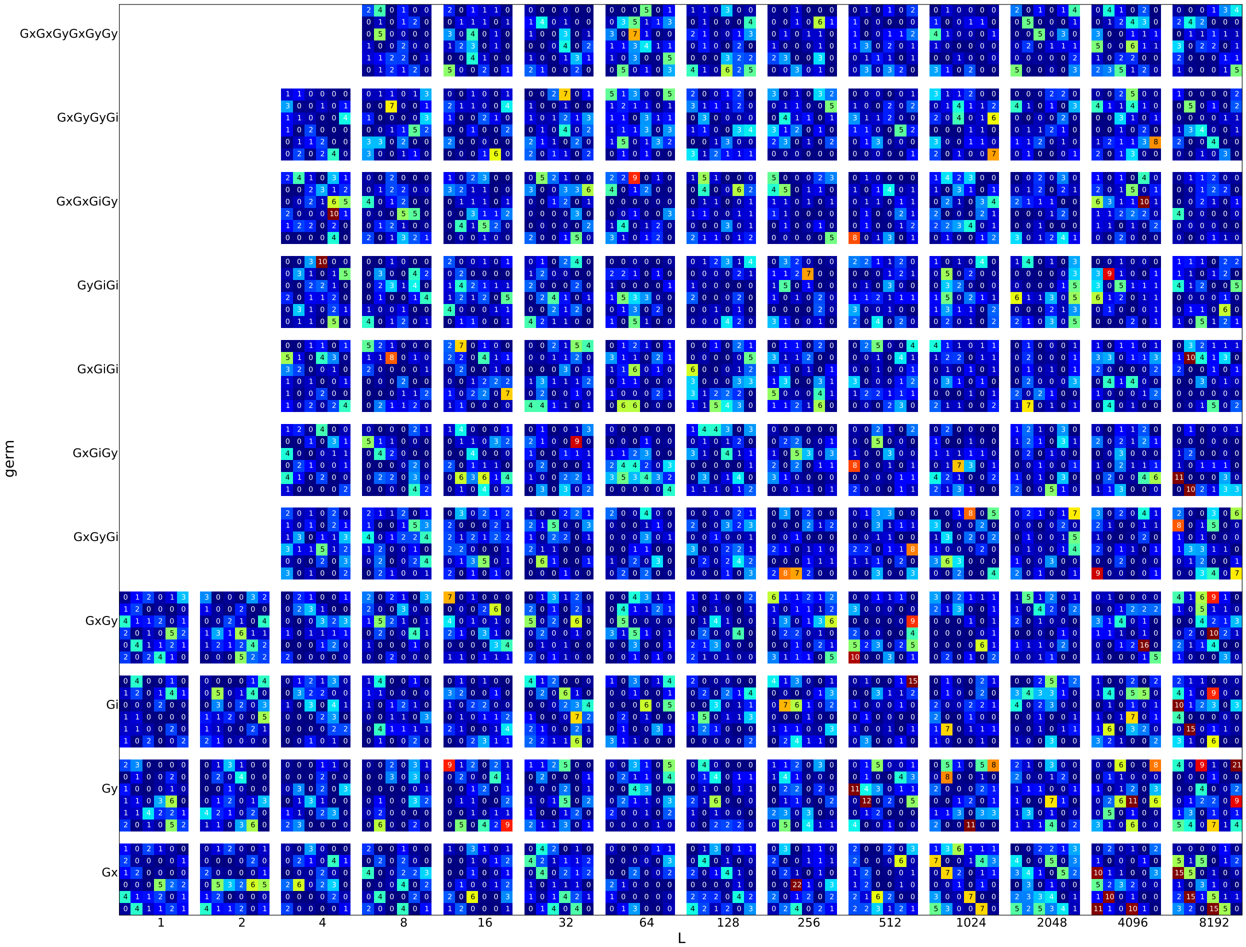

Figure A.4. $2\Delta\log(\mathscr{L})$ **contributions for every individual experiment in the dataset**. Each pixel represents a single experiment (gate sequence), and its color indicates whether GST was able to fit the corresponding frequency well. Blue is typical; dark red squares indicating $2\Delta\log(\mathscr{L})_s > 10$ should appear only once per 638 experiments on average. Square blocks of pixels correspond to base sequences (arranged vertically by germ and horizontally by length); each pixel within a block corresponds to a specific choice of pre- and post-fiducial sequences. See text for further details.

Gate	Eigenvalues	Fixed pt	Rotn. axis	Diag. decay	Off-diag. decay
Gi	0.9999 ± 0.0002	1	0		
	$0.9999e^{i0.0} \pm 0.0001e^{i0.3}$	0	$0.7557e^{i0.1}$	0.000082	0.000082
	$0.9999e^{-i0.0} \pm 0.0001e^{i0.3}$	0	$0.6085e^{-i1.2}$	± 0.000151	± 0.00032
	1 ± 0	0	$0.242e^{i0.6}$		
Gx	$0.9999e^{i1.6} \pm 0.0082e^{i0.0}$	1	0		
	$0.9999e^{-i1.6} \pm 0.0082e^{i0.0}$	-9×10^{-9}	1	0.000051	0.000095
	$0.9999 \pm 8 \times 10^{-6}$	0.0009	-9×10^{-6}	± 0.000008	± 0.000011
	1 ± 0	0.0016	1×10^{-5}		
Gy	$0.9999e^{i1.6} \pm 0.0037e^{i0.0}$	1	0		
	$0.9999e^{-i1.6} \pm 0.0037e^{i0.0}$	-0.0002	1×10^{-5}	0.000042	0.000109
	$1 \pm 7 \times 10^{-6}$	5×10^{-7}	1	± 0.000007	± 0.000008
	1 ± 0	0.0017	-0.0003		

Gate	Angle	Angle between Rotation Axes		
		Gi	Gx	Gy
Gi	$(0 \pm 0.008155)\pi$		–	–
Gx	$(0.499977 \pm 0.004078)\pi$	–		0.499999π
Gy	$(0.499999 \pm 0.001864)\pi$	–	0.499999π	

Table A.8. Eigen-decomposition of estimated gates. Each estimated gate is described in terms of: (1) the eigenvalues of the superoperator; (2) the gate's fixed point (as a vector in $\mathscr{B}(\mathscr{H})$, in the Pauli basis); (3) the axis around which it rotates, as a vector in $\mathscr{B}(\mathscr{H})$; (4) the angle of the rotation that it applies; (5) the decay rate along the axis of rotation ("diagonal decay"); (6) the decay rate perpendicular to the axis of rotation ("off-diagonal decay"); and (7) the angle between each gate's rotation axis and the rotation axes of the other gates. "X" indicates that the decomposition failed or couldn't be interpreted.

DISTRIBUTION:

1	MS 0672	Han Wei Lin, 5629 (electronic copy)
1	MS 1082	Michael Descour, 1725 (electronic copy)
1	MS 1322	John Aidun, 1425 (electronic copy)
1	MS 0359	D. Chavez, LDRD Office, 1911 (electronic copy)
1	MS 0899	Technical Library, 9536 (electronic copy)

Sandia National Laboratories